Science
AAAS

Fast and destructive density currents created by ocean-entering volcanic eruptions

Michael A. Clare[1]†, Isobel Yeo[1]†, Sally Watson[2], Richard Wysoczanski.[2], Sarah Seabrook[2], Kevin Mackay[2], James. E. Hunt[1], Emily Lane[2], Peter J. Talling[3], Edward Pope[3], Shane Cronin[4], Marta Ribó[5], Taaniela Kula[6], David Tappin[7], Stuart Henrys[8], Cornel de Ronde[8], Morelia Urlaub[9], Stefan Kutterolf[9], Samiuela Fonua[10], Semisi Panuve[10], Dean Veverka[11], Ronald Rapp[12], Valey Kamalov[13], Michael Williams[2]

[1]National Oceanography Centre, Southampton, UK
[2]National Institute of Water and Atmospheric Research (NIWA), Auckland, Aotearoa New Zealand
[3]Department of Geography and Department of Earth Sciences, Durham University, Durham, UK
[4]School of Environment, University of Auckland, Auckland, Aotearoa New Zealand
[5]Department of Environmental Science, Auckland University of Technology, Auckland, Aotearoa New Zealand
[6]Ministry of Lands and Natural Resources, Nuku'alofa, Kingdom of Tonga;
[7]British Geological Survey, Keyworth, UK
[8]GNS Science, Lower Hutt, Aotearoa New Zealand
[9]GEOMAR Helmholtz Centre for Ocean Research Kiel, Kiel, Germany
[10]Tonga Cable Ltd, Nuku'alofa, Kingdom of Tonga
[11]Southern Cross Cable Network, North Ryde, New South Wales, Australia
[12]SubCom, Newington, NH, USA
[13]Valey Kamalov LLC, Gainsville, Florida, USA

Corresponding author. Email: michael.clare@noc.ac.uk (M.A.C.) and i.yeo@noc.ac.uk (I.Y.)
†These authors contributed equally to this work.

Abstract: Volcanic eruptions on land create hot and fast pyroclastic density currents, triggering tsunamis or surges that travel over water where they reach the ocean. However, no field study has documented what happens when large volumes of erupted volcanic material are instead delivered directly into the ocean. We show how the rapid emplacement of large volumes of erupted material onto steep submerged slopes triggered extremely fast (122 km/hr) and long runout (>100 km) seafloor currents. These density currents were faster than those triggered by earthquakes, floods or storms, and broke seafloor cables, cutting off a nation from the rest of the world. The deep scours excavated by these currents are similar to those around many submerged volcanoes, providing evidence of large eruptions at other sites worldwide.

Explosive volcanism poses a wide range of hazards, with more than a third of volcanic fatalities attributed to fast (up to 100s of km/hour) and high temperature pyroclastic density currents triggered by: phreatic explosions; pyroclastic fountaining; lateral blasts; caldera- and dome-collapses; and the vertical collapse of eruption columns where they impact the ground *(1, 2, 3, 4, 5, 6)*. Study of the behavior of pyroclastic density currents on land has revealed a spectrum from dense to dilute and turbulent modes of flow, across which a range of hazards exists *(1,2,3)*. This spectrum also relates to other types of particulate density currents, including snow avalanches and underwater sediment-laden flows called turbidity currents *(e.g. 7, 8, 9)*. Where terrestrially-initiated pyroclastic density currents reach the ocean, they create different hazards. Such currents can generate tsunamis, create phreatic explosions as hot currents interact with water, travel over the sea, and/or rapidly cool and transition into a turbidity current, damaging seafloor infrastructure and devastating marine biological communities *(10, 11, 12, 13, 14, 15)*.

Repeat terrestrial surveys and sampling after the occurrence of pyroclastic density currents have enabled reconstruction of flow properties from the resultant deposits to understand the associated hazards (e.g.*16, 17, 18*). However, field-scale observations of density currents linked to volcanic eruptions in marine settings are rare, due to often-remote locations and inaccessibility of in-situ deposits. The behavior of terrestrially-initiated pyroclastic density currents that cross land to enter the ocean has only been documented at a single field site following a small (0.19 km^3) eruption *(12, 13, 14)*, while no equivalent study has shown what happens when an eruption directly delivers volcanic material into the ocean. We address this knowledge gap with new observations of underwater volcaniclastic density currents triggered during the eruption of the partially-submerged Hunga Tonga-Hunga Ha'apai (hereafter Hunga volcano) volcano in The Kingdom of Tonga. We use the term 'volcaniclastic density current', which encompasses a spectrum of density currents linked to a volcanic eruption, from hot gas-supported pyroclastic density currents to cold fluid-supported turbidity currents.

A key control on the hazard posed by any type of density current is their velocity *(9, 19, 20, 21, 22)*. While recent advances in technology enabled the direct measurement of turbidity currents and snow avalanches, no velocity measurements exist for underwater volcaniclastic density currents *(9, 19, 20, 21)*. These limitations are remarkable, considering the distinct hazards posed by partially or fully-submerged volcanoes, which account for more than three quarters of active volcanoes worldwide *(6)*. Consequently, our knowledge relies on studies of ancient ocean-entering eruptions (*23, 24*), scaled-down laboratory modelling (*25*), and analysis of geomorphic features around submerged volcanoes to infer the behavior of past eruptions (*26, 27*). Fields of large sediment waves and scours, commonly observed radiating around submerged flanks of volcanoes, are thought to be diagnostic of catastrophic eruptions *(26, 27, 28)*. However, this hypothesis remains untested due to a lack of repeat seafloor surveys before and after a large eruption. These uncertainties severely limit the understanding of the behavior and associated risks at submerged volcanoes.

We present new observations of voluminous volcaniclastic density currents that were triggered by the January 15th 2022 eruption of Hunga volcano in The Kingdom of Tonga. This eruption was the most explosive in over a century and had worldwide impacts *(29, 30, 31, 32, 33, 34, 35)*. The eruption plume entered the mesosphere (57 km high), tsunamis travelled across the Pacific Ocean and caused 19-20 m runups in Tonga, while a pressure wave encircled the globe multiple times *(29, 30, 31, 33, 34)*. More than one hour after the main eruption, Tonga's only international subsea telecommunications cable was severed (Fig 1), disconnecting the entire nation from global digital

communications at a critical time for disaster response *(36)*. Such an incident has wider implications because subsea cables carry >99% of all international data traffic, including the internet and trillions of dollars per day in financial transactions *(37)*. The >6 km^3 eruption expelled an equivalent volume of material to the annual sediment flux from all the world's rivers combined, much of which directly entered the ocean via eruption column collapses *(15, 38)*. The rapid escalation in explosivity and the resultant hazards were unexpected, exposing a gap in understanding of many similar, yet un-monitored volcanoes along the Tonga-Tofua Arc and volcanic settings worldwide *(6, 29, 30, 39)*.

By integrating datasets that document their timing and extent, we determined the behavior of underwater volcaniclastic density currents triggered by the 2022 eruption of Hunga volcano. These currents travelled over 100 km and caused extensive damage to seafloor cables from which we could estimate their velocity, which was up to 122 km/hour. These currents differ markedly from those triggered by terrestrially-initiated pyroclastic density currents that enter the ocean, and their velocity is higher than that recorded for other underwater density currents, including those triggered by terrestrial flood, large earthquakes, or ocean waves (Table 1). The currents created distinctive scours around Hunga volcano, excavating regions over 100 m deep into the volcanic edifice (Fig 2); evident by comparing surveys three months after the eruption to pre-eruption surveys performed in 2016. Bedforms like these are generated by, and thus probably record, large explosive eruptions.

Extensive damage to seafloor cables

At 03:47 (all times UTC) on 15th January 2022, a low eruptive plume was observed at Hunga volcano, marking the onset of the main eruptive phase, with a steady narrow plume rising to >10 km height (*34*) (Fig 1). At 04:15 (T_{0a}), a large explosion occurred (Volcanic Explosivity Index of 5-6 (*35*)), which transformed the plume. High eruption rates rapidly increased the height and width of an expanding umbrella-shaped eruption plume (*34; Fig S6*). The plume reached 16-18 km height at 04:17. A second major explosion (T_{0b}) occurred at 04:21, with further explosions generating sonic booms until 04:25 (inception of the atmospheric pressure wave). By this time, the umbrella cloud expanded to at least 120 km-wide and the central plume was >15 km-wide. Plume collapses into the ocean below the umbrella cloud occurred soon after 04:17, especially from 04:20 onward(Fig S6 (*34)*). By 04:50-04:55, the central high plume ceased rising and was dispersed by the wind. However, the eruption continued vigorously with a lower plume (~17-21 km high) formed beneath the larger 57 km high plume.

Both subsea cables were broken on 15th January, but the timing of this damage lagged after the two most intense explosions (T_{0a} & T_{0b}) by 9-15 minutes for the domestic (at 04:30) and 83-89 minutes for the international cable (05:44) (Table S1). The timing of these breaks is known to the nearest minute, based on loss of data transmission, ultimately with complete loss of Internet capacity when the international cable was severed. The distance of the first point of cable damage from shore was determined immediately using Optical Time Domain Reflectometry, but the full extent could not be assessed until a cable repair ship retrieved the intact ends of the cable either side of the damaged zone. The international cable repair took five weeks, as the closest repair ship was 2500 km away in Papua New Guinea and over 100 km of replacement cable was required. Communications were limited across the Kingdom, until the domestic cable was finally repaired, 18 months after the eruption.

Prior to repair, cable damage was thought to be caused by local seabed landslides; however, the extent of damage was far greater than anticipated. More than 89 km of the international cable was broken and/or buried to a depth beyond recovery, while 105 km of the domestic cable was affected. Moreover, the international cable was recovered at a distance of 5 km to the north of its originally laid position, towards the volcano. This incident was the largest length of cable damage since telegraph cables were buried by the >200 km^3 Grand Banks landslide offshore Newfoundland in 1929 *(40)* and the longest single cable repair in the modern fibre-optic era (Fig 1). We did not find evidence within the resolution of imaging of slope failures on the deep-water volcano flanks around the cables and surrounding slopes. We therefore relate the cable damage to powerful and long run-out volcaniclastic density currents triggered by the effective delivery of large volumes of erupted pyroclastic material directly into the ocean.

Insights into underwater density currents triggered by eruption column collapse

Dense and highly erosive proximal regime: Linear gullies and trains of crescentic scours, incised up to 100 m, radiate from the caldera (Fig 2), accounting for 3.5 km^3 of erosion(*15)* and representing an additional removed mass of over 50% of the original erupted volume. Erosional features include up to 2 km-wide scours and upslope-asymmetric bedforms (30-60 m wave height, 500-2000 m wavelength) seen in pre-eruption surveys, which migrated up to 1.5 km upslope. Pronounced erosion observed from the post-eruption survey, occurs within a radius of <9.2 km from the caldera rim and only on the steepest slopes (>10^o, locally >40^o; Fig 2). Recovery of material by seafloor coring was not successful on such proximal slopes, presumably due to presence of competent volcanic rock and/or coarse granular material. Deposition occurs as slope angles reduce (<10^o), where well-defined lobes (up 40 m-thick and 7 km-wide) accumulated downstream of two of the erosional chutes. As this lobate deposition occurs on relatively steep slopes, a dense granular current with high basal friction was likely responsible for the proximal depositional lobes *(41, 42, 43)*. This is in stark contrast to turbidity currents, which typically do not deposit on steep slopes, or where they do, leave only very thin deposits (*44*). Indeed, some turbidity currents only deposit on slopes of less than 0.05^o (*45*).

The intense erosion on steep slopes (Fig 2) caused currents to increase their sediment mass substantially, thereby enhancing their power and mobility (*47*). For context, the eroded volume is 0.5 km^3 greater than the largest known historical volcanic landslide (3 km^3; Mt St Helens (*47*)) and ~1 km^3 greater than the sediment volume eroded by the longest monitored turbidity current that travelled >1000 km along the deep-sea Congo Canyon (*19*). Stepped trains of upslope-migrating crescentic scours and large-scale bedforms on steep slopes evidence Froude-supercritical currents undergoing a series of hydraulic jumps (*48, 49, 50)*. Similar scours and bedforms are a common feature proximal to the initiation of other large volume particulate density currents, including those in non-volcanic settings (e.g. 1 km^3 earthquake-triggered turbidity current in Kaikōura Canyon (*51)*) and are of similar scale to those thought to diagnose past large explosive eruptions on submerged volcanic flanks (*25, 26, 27, 28*) (Fig 2H). We confirm this previously-hypothesised link, showing that multiple radial chutes and bedforms can be formed during an individual explosive eruption, which has important implications for assessing hazards from seabed geomorphology at other submerged volcanoes worldwide.

Depositional distal regime: The remaining surveyed area is characterised by widespread, relatively-featureless blanketed deposition, with an average of +2.8 m elevation change (i.e. net-depositional). In the valley south-east of Hunga volcano (location of the domestic cable), slopes rapidly reduce to under 1.5^o, and ponded deposition occurred (up to 27 m thick). Even where

elevation change was not resolvable from repeat seafloor surveys in deep-water, sampling (up to 108 km from the caldera) recovered volcaniclastic deposits emplaced by density currents (Fig 1). Density current deposits are generally decimeter-thickness and comprise sand-granule-sized volcanic material that fines upwards, with internal lamination, ripples and sharp bases, and are geochemically-linked to the 2022 Hunga volcanic eruption *(16)*. Those deposits are overlain by thinner deposits interpreted as ash fall-out ((*53*) Fig S2; Table S2). The area around the international cable was not covered by pre-existing bathymetric data; however, detailed seafloor backscatter data reveals trains of bedforms (1-2 m wave height, 100-200 m wavelength) within a valley between seamounts (Fig S1). These bedforms evidence a complex flow pathway as corroborated by earlier modelling *(15*). So dramatic was the topographic steering, that the cable was moved 5 km towards the volcano by the density current (Fig S1).

Contrasting behavior of underwater volcaniclastic density currents

These depositional/erosional patterns contrast with observations from repeat seafloor surveys and sampling of terrestrially-initiated pyroclastic density currents that entered the ocean offshore Montserrat in the Caribbean (*12, 13, 14*). Deposits offshore Montserrat formed in two parts: (i) coarse-grained ridges up to 60 m-thick within 3-4 km of the ocean-entry point formed by a dense granular current; and (ii) a broader deep-water lobe, comprising centimeters-thick fine-grained deposits related to a dilute turbidity current (*12, 13, 14)*. The proximal deposition of ridges offshore Montserrat contrasts with the erosional chutes, scours and asymmetric bedforms we observe on Hunga volcano. Further, the lobes at Hunga volcano are much higher relief, thicker (tens of meters rather than centimeters-thick), on steeper slopes (up to 8-10^{o} cf. <2^{o}), and likely comprise coarser material, with deposits sampled at least 108 km from the edifice, compared to 40 km offshore Montserrat (Fig 1). Seafloor cores show coarse granular deposits were deposited at least 80 km from the Hunga edifice, indicating currents maintained high densities over this distance, also in contrast with the dilute flow origin for distal finer-grained deposits offshore Montserrat *(12, 13, 14)*.

Fast and long run-out underwater volcaniclastic density currents

Large volumes of pyroclastic material were delivered into the ocean during the eruption at Hunga volcano, creating dense underflows that were steered down its steep flanks. It is most likely that the pyroclastic material was predominantly derived from partial collapses of the eruption column, but we cannot fully preclude that currents may have been fed in part by other eruption processes, including jetting or fountaining. Initially, these volcaniclastic density currents would have been a dominantly gas-particle mixture, then transitioned into a water-particle mixture as they cooled and mixed with seawater (*23*). We cannot discern the precise extent of that transition, underlining our broader use of *volcaniclastic* rather than *pyroclastic* density current. Volcaniclastic density currents were initially steered along pre-existing relief into a valley 15 km southeast of the caldera. In this location, currents impacted the domestic cable side-on, and were deflected to the north and south (i.e. parallel to the cable) by the topography. Based on the time between the first collapses of the eruptive column into the ocean (T_{0a} & T_{0b}) and cutting of the domestic cable, we calculate a distance-averaged transit (front) flow velocity of 63-122 km/hour (17.6-38.8 m/s; Table S1). This observation is remarkable, given the inherent challenges in underwater monitoring, particularly during an ongoing large eruption.

Despite the higher resistance provided by the surrounding seawater compared to air, the velocities of volcaniclastic density currents offshore from Hunga volcano fall within the range measured for pyroclastic density currents on land *(e.g.20)* (Table S4). The velocities at Hunga volcano are higher

than previously documented for underwater density currents elsewhere in the ocean, including turbidity currents triggered by large magnitude earthquakes, river floods and oceanographic processes (Table 1; Fig 3). The fastest transit velocities for turbidity currents are up to 72 km/hour (20 m/s; based on cable breaks during the 1929 Grand Banks landslide (*40*) and the 2006 Pingtung earthquake offshore Taiwan (*37*)). The volcaniclastic density currents at Hunga volcano were steered into deeper water along tortuous paths created by irregular volcanic topography, where they severed the international cable 70 km from the volcano (Fig. 1). Assuming this current was the same one that also broke the domestic cable, indicates a transit velocity of 32-51 km/hour (8.9-14.2 m/s). This is remarkably fast given the distance travelled. However, our data do not enable us to determine how many currents were triggered at Hunga volcano. It is plausible that damage to the international cable resulted from currents triggered by eruption collapses considerably later in the eruption cycle (i.e. after T_{0a} and conceivably after T_{0b}), and in which case these distal velocities are underestimates.

What explains the fast current speeds?

The sheer mass and manner of delivery of material to the ocean (i.e. direct and rapid vertical entry of a fast-collapsing plume) at Hunga volcano is distinct to other mechanisms for particulate density current generation, such as river plumes that enter the ocean laterally, and landslide-triggered turbidity currents that initiate on far lower angle slopes and where material in the parent flow must first disintegrate and mix (Fig 3). The dominantly downward rather than lateral trajectory towards and through the air-ocean boundary, also make the ocean-entry mechanism of dense pyroclastic material at Hunga volcano distinct from terrestrially-initiated, ocean-entering pyroclastic density currents such as observed at Montserrat. The pyroclastic density currents that entered the ocean at Montserrat, first travelled 4 km laterally over land, along the Tar River valley following a dome collapse *(12, 13, 14)*. Instead, the formative mechanism at Hunga volcano is better described as a vertical jet or fountain collapse of a gas-particle mixture (*52*), wherein a huge sediment load of dense volcanic pyroclasts (up to 2.8 g/cm^3(*53)*) fell vertically from considerable height (several kms) as the eruption column collapsed into the ocean (Fig 3).

According to the modified Chézy equation (a simplified approach often used to model behavior of turbidity currents(*53*)), to maintain the high current velocities observed at Hunga volcano requires a combination of a steep slope, thick current, and/or high sediment concentrations (expressed as the 'depth averaged' value for a vertical profile through the current *(54, 53)*. Assuming previously-accepted basal and upper friction values for underwater density currents*(54*), to attain the high transit velocities on the edifice flanks requires current thicknesses on the order of tens of meters, with depth-averaged sediment concentrations of up to 5%, or else even thicker currents (e.g. hundreds of meters) with lower depth-averaged sediment concentrations (1-2% $conc_{vol}$). Near-bed sediment concentrations are likely substantially higher than these depth-averaged values (*8,55*). These concentrations are particularly high for underwater particulate density currents (e.g.*55*), as evidenced by the deposition of lobes on steep (up to ~10^o) slopes of the edifice, implying a dense granular basal layer (*41, 42, 43*). Currents at Hunga volcano had sufficient inertia to flow upslope in some areas (and overtop relief of up to 860 m), such as south of the domestic cable break and to reach the international cable Fig S4&5). This inertia was provided by their initial velocity and concentration, and additional entrained mass due to the substantial seafloor erosion. We conclude that fast velocities proximal to Hunga volcano result from: i) the potential energy generated from the direct, vertical entry of dense and large volume pyroclastic fluxes into the ocean; ii) the extremely steep (up to 45^o) submerged edifice flanks, which were the location of the impact zone

for the collapsed material (*52*); and iii) the additional mass gained by the currents as they eroded into the edifice flanks.

Implications for hazards assessment

A push to enhance telecommunications links across the South Pacific and Caribbean will necessitate the crossing of volcanically-active regions by new subsea cable routes with a need to assess threats posed to remote coastal communities and the international communications infrastructure that serve them. This requires more extensive seafloor mapping to identify submerged volcanoes that may experience similar eruptions, while offshore monitoring, such as using fiber-optic sensing along telecommunications cables *(e.g.56, 57)*, is required to provide early-warning. We show that volcaniclastic density currents triggered when an eruption collapses into the ocean can maintain high densities over distances of over 100 km and attain speeds up to 122 km/hour, providing a fundamentally new view of their behavior and associated hazards. We confirm that bedforms observed on many other shallow submerged volcanoes worldwide can be produced by powerful eruptions, demonstrating the hazards experienced at Hunga volcano can occur elsewhere (*4, 8, 27*). Explosive eruptions from these often un-surveyed and un-monitored, submerged volcanoes can produce high-energy submarine density currents and warrant far greater consideration as tsunamigenic sources as well as primary threats to vulnerable coastal communities and critical subsea infrastructure.

REFERENCES AND NOTES

References

1 Lube, G., Breard, E.C., Esposti-Ongaro, T., Dufek, J. and Brand, B., 2020. Multiphase flow behaviour and hazard prediction of pyroclastic density currents. Nature Reviews Earth & Environment, 1(7), pp.348-365.

2 Breard, E.C., Lube, G., Jones, J.R., Dufek, J., Cronin, S.J., Valentine, G.A. and Moebis, A., 2016. Coupling of turbulent and non-turbulent flow regimes within pyroclastic density currents. Nature Geoscience, 9(10), pp.767-771.

3 Breard, E.C. and Lube, G., 2017. Inside pyroclastic density currents–uncovering the enigmatic flow structure and transport behaviour in large-scale experiments. Earth and Planetary Science Letters, 458, pp.22-36.

4 de Ronde, C.E.J., Massoth, G.J., Baker, E.T. & Lupton, J.E., 2003, Submarine hydrothermal venting related to volcanic arcs, In, Giggenbach Memorial volume, S.F. Simmons and I.G Graham (eds.). Society of Economic Geology and Geochemical Society Special Publication 10, 91-109.

5 Auker, M.R., Sparks, R.S.J., Siebert, L., Crosweller, H.S. and Ewert, J., 2013. A statistical analysis of the global historical volcanic fatalities record. Journal of Applied Volcanology, 2, pp.1-24.

6 Mastin, L.G. and Witter, J.B., 2000. The hazards of eruptions through lakes and seawater. Journal of Volcanology and Geothermal Research, 97(1-4), pp.195-214.

7 Sovilla, B., Schaer, M., Kern, M. and Bartelt, P., 2008. Impact pressures and flow regimes in dense snow avalanches observed at the Vallée de la Sionne test site. Journal of Geophysical Research: Earth Surface, 113(F1).

8 Pope, E.L., Cartigny, M.J., Clare, M.A., Talling, P.J., Lintern, D.G., Vellinga, A., Hage, S., Açikalin, S., Bailey, L., Chapplow, N. and Chen, Y., 2022. First source-to-sink monitoring shows dense head controls sediment flux and runout in turbidity currents. Science Advances, 8(20), p.eabj3220.

9 Sovilla, B., McElwaine, J.N. and Louge, M.Y., 2015. The structure of powder snow avalanches. Comptes Rendus Physique, 16(1), pp.97-104.

10 Sparks, R.S.J., Sigurdsson, H. and Carey, S.N., 1980. The entrance of pyroclastic flows into the sea I. Oceanographic and geologic evidence from Dominica, Lesser Antilles. Journal of Volcanology and Geothermal Research, 7(1-2), pp.87-96.

11 Carey, S., Sigurdsson, H., Mandeville, C. and Bronto, S., 2000. Volcanic hazards from pyroclastic flow discharge into the sea: examples from the 1883 eruption of Krakatau, Indonesia. Special Papers-Geological Society of America, pp.1-14.

12 Trofimovs, J., Amy, L., Boudon, G., Deplus, C., Doyle, E., Fournier, N., Hart, M.B., Komorowski, J.C., Le Friant, A., Lock, E.J. and Pudsey, C., 2006. Submarine pyroclastic deposits formed at the Soufrière Hills volcano, Montserrat (1995–2003): What happens when pyroclastic flows enter the ocean?. Geology, 34(7), pp.549-552.

13 Trofimovs, J., Sparks, R.S.J. and Talling, P.J., 2008. Anatomy of a submarine pyroclastic flow and associated turbidity current: July 2003 dome collapse, Soufrière Hills volcano, Montserrat, West Indies. Sedimentology, 55(3), pp.617-634.

14 Trofimovs, J., Foster, C., Sparks, R.S.J., Loughlin, S., Le Friant, A., Deplus, C., Porritt, L., Christopher, T., Luckett, R., Talling, P.J. and Palmer, M.R., 2012. Submarine pyroclastic deposits formed during the 20th May 2006 dome collapse of the Soufriere Hills Volcano, Montserrat. Bulletin of Volcanology, 74(2), pp.391-405.

15 Seabrook, S., Mackay, K., Watson, S., Clare, M., Hunt, J., Yeo, I., Lane, E., Clark, M., Wysoczanski, R., Rowden, A. and Hoffmann, L., 2023. Pyroclastic density currents explain far-reaching and diverse seafloor impacts of the 2022 Hunga Tonga Hunga Ha'apai eruption. Research Square. DOI: https://doi.org/10.21203/rs.3.rs-2395332/v

16 Gomez, C., Lavigne, F., Hadmoko, D.S., Lespinasse, N. and Wassmer, P., 2009. Block-and-ash flow deposition: a conceptual model from a GPR survey on pyroclastic-flow deposits at Merapi Volcano, Indonesia. Geomorphology, 110(3-4), pp.118-127.

17 Jessop, D.E., Kelfoun, K., Labazuy, P., Mangeney, A., Roche, O., Tillier, J.L., Trouillet, M. and Thibault, G., 2012. LiDAR derived morphology of the 1993 Lascar pyroclastic flow deposits, and implication for flow dynamics and rheology. Journal of Volcanology and Geothermal Research, 245, pp.81-97.

18 Hofton, M.A., Malavassi, E. and Blair, J.B., 2006. Quantifying recent pyroclastic and lava flows at Arenal Volcano, Costa Rica, using medium-footprint lidar. Geophysical Research Letters, 33(21).

19 Talling, P.J., Baker, M.L., Pope, E.L., Ruffell, S.C., Jacinto, R.S., Heijnen, M.S., Hage, S., Simmons, S.M., Hasenhündl, M., Heerema, C.J., McGhee, C., Apprioual, R., Ferrant, A., Cartigny, M.J.B., Parsons, D.R., Clare, M.A., Tshimanga, R.M., Trigg, M.A., Cula, C.A., Faria, R., Gaillot, A., Bola, G., Wallace, D., Griffiths, A., Hilton, R. 2022. Longest sediment flows yet measured show how major rivers connect efficiently to deep sea. Nature communications, 13(1), p.4193.

20 Scharff, L., Hort, M. and Varley, N.R., 2019. First in-situ observation of a moving natural pyroclastic density current using Doppler radar. Scientific Reports, 9(1), pp.1-9.

21 Valentine, G.A., 1998. Damage to structures by pyroclastic flows and surges, inferred from nuclear weapons effects. Journal of Volcanology and Geothermal Research, 87(1-4), pp.117-140.

22 Vilajosana, I., Khazaradze, G., Surinach, E., Lied, E. and Kristensen, K., 2007. Snow avalanche speed determination using seismic methods. Cold regions science and technology, 49(1), pp.2-10.

23 Kokelaar, P., Raine, P. and Branney, M.J., 2007. Incursion of a large-volume, spatter-bearing pyroclastic density current into a caldera lake: Pavey Ark ignimbrite, Scafell caldera, England. Bulletin of Volcanology, 70, pp.23-54.

24 Kokelaar, P. and Koniger, S., 2000. Marine emplacement of welded ignimbrite: the Ordovician Pitts Head Tuff, North Wales. Journal of the Geological Society, 157(3), pp.517-536.

25 Gilchrist, J.T., Jellinek, A.M., Hooft, E.E. and Wanket, S., 2023. Submarine terraced deposits linked to periodic collapse of caldera-forming eruption columns. Nature Geoscience, pp.1-8.

26 Pope, E.L., Jutzeler, M., Cartigny, M.J., Shreeve, J., Talling, P.J., Wright, I.C. and Wysoczanski, R.J., 2018. Origin of spectacular fields of submarine sediment waves around volcanic islands. Earth and Planetary Science Letters, 493, pp.12-24.

27 Casalbore, D., Clare, M.A., Pope, E.L., Quartau, R., Bosman, A., Chiocci, F.L., Romagnoli, C. and Santos, R., 2021. Bedforms on the submarine flanks of insular volcanoes: New insights gained from high resolution seafloor surveys. Sedimentology, 68(4), pp.1400-1438.

28 Karstens, J., Preine, J., Carey, S., Bell, K.L., Nomikou, P., Hübscher, C., Lampridou, D. and Urlaub, M., 2023. Formation of undulating seafloor bedforms during the Minoan eruption and their implications for eruption dynamics and slope stability at Santorini. Earth and Planetary Science Letters, 616, p.118215.

29 Borrero, J.C., Cronin, S.J., Latu'ila, F.H., Tukuafu, P., Heni, N., Tupou, A.M., Kula, T., Fa'anunu, O., Bosserelle, C., Lane, E. and Lynett, P., 2022. Tsunami runup and inundation in Tonga from the January 2022 eruption of Hunga Volcano. Pure and applied geophysics, pp.1-22.

30 Lynett, P., McCann, M., Zhou, Z., Renteria, W., Borrero, J., Greer, D., Fa'anunu, O., Bosserelle, C., Jaffe, B., La Selle, S. and Ritchie, A., 2022. Diverse tsunamigenesis triggered by the Hunga volcano eruption. Nature, 609(7928), pp.728-733.

31 Pakoksung, K., Suppasri, A. and Imamura, F., 2022. The near-field tsunami generated by the 15 January 2022 eruption of the Hunga volcano volcano and its impact on Tongatapu, Tonga. Scientific reports, 12(1), pp.1-15.

32 Poli, P. & Shapiro, N. M. Rapid characterization of large volcanic eruptions: measuring the impulse of the Hunga Tonga Ha'apai explosion from teleseismic waves. Geophys. Res. Lett. 49, e2022GL098123 (2022).

33 Proud, S.R., Prata, A.T. and Schmauß, S., 2022. The January 2022 eruption of Hunga volcano volcano reached the mesosphere. Science, 378(6619), pp.554-557.

34 Purkis, S. J., Ward, S. N., Fitzpatrick, N. M., Garvin, J. B., Slayback, D., Cronin, S. J., Palaseanu-Lovejoy, M., & Dempsey, A. (2023). The 2022 Hunga-Tonga megatsunami: Near-field simulation of a once-in-a-century event. Science Advances, 9(15), eadf5493. https://doi.org/doi:10.1126/sciadv.adf5493

35 Yuen, D.A., Scruggs, M.A., Spera, F.J., Zheng, Y., Hu, H., McNutt, S.R., Thompson, G., Mandli, K., Keller, B.R., Wei, S.S. and Peng, Z., 2022. Under the surface: Pressure-induced planetary-scale waves, volcanic lightning, and gaseous clouds caused by the submarine eruption of Hunga Tonga-Hunga Ha'apai volcano. Earthquake Research Advances, 2(3), p.100134.

36 The World Bank and the Global Facility for Disaster Reduction and Recovery, 2022. The January 15, 2022 Hunga Tonga-Hunga Ha'Apai eruption and tsunami, Tonga: Global rapid post disaster damage estimation (grade) report in partnership with the Government of Tonga, https://thedocs.worldbank.org/en/doc/b69af83e486aa652d4232276ad698c7b-0070062022/original/GRADE-Report-Tonga-Volcanic-Eruption.pdf

37 Carter, L., Gavey, R., Talling, P.J. and Liu, J.T., 2014. Insights into submarine geohazards from breaks in subsea telecommunication cables. Oceanography, 27(2), pp.58-67.

38 Syvitski, J., Ángel, J.R., Saito, Y., Overeem, I., Vörösmarty, C.J., Wang, H. and Olago, D., 2022. Earth's sediment cycle during the Anthropocene. Nature Reviews Earth & Environment, 3(3), pp.179-196.

39 Cassidy, M. and Mani, L., 2022. Huge volcanic eruptions: Time to prepare. Nature, 608(7923), pp.469-471.

40 Heezen, B.C., Ericson, D.B. and Ewing, M., 1954. Further evidence for a turbidity current following the 1929 Grand Banks earthquake. Deep Sea Research (1953), 1(4), pp.193-202.

41 Iverson, R.M., 1997. The physics of debris flows. Reviews of geophysics, 35(3), pp.245-296.

42 Iverson, R.M. and Vallance, J.W., 2001. New views of granular mass flows. Geology, 29(2), pp.115-118.

43 Major, J.J., 1997. Depositional processes in large-scale debris-flow experiments. The Journal of Geology, 105(3), pp.345-366.

44 Stevenson, C.J., Jackson, C.A.L., Hodgson, D.M., Hubbard, S.M. and Eggenhuisen, J.T., 2015. Deep-Water Sediment Bypass. Journal of Sedimentary Research, 85(9), pp.1058-1081.

45 Talling, P.J., Wynn, R.B., Masson, D.G., Frenz, M., Cronin, B.T., Schiebel, R., Akhmetzhanov, A.M., Dallmeier-Tiessen, S., Benetti, S., Weaver, P.P.E. and Georgiopoulou, A., 2007. Onset of submarine debris flow deposition far from original giant landslide. Nature, 450(7169), pp.541-544.

46 Manganet A. Mangeney, Olivier Roche, O. Hungr, N. Mangold, Gloria Faccanoni, et al.. Erosion and mobility in granular collapse over sloping beds. Journal of Geophysical Research : Solid Earth, 2010, 115 (F3), pp.F03040. ff10.1029/2009JF001462ff.

47 Korup, O., Clague, J.J., Hermanns, R.L., Hewitt, K., Strom, A.L. and Weidinger, J.T., 2007. Giant landslides, topography, and erosion. Earth and Planetary Science Letters, 261(3-4), pp.578-589.

48 Cartigny, M.J., Ventra, D., Postma, G. and van Den Berg, J.H., 2014. Morphodynamics and sedimentary structures of bedforms under supercritical-flow conditions: new insights from flume experiments. Sedimentology, 61(3), pp.712-748.

49 Symons, W.O., Sumner, E.J., Talling, P.J., Cartigny, M.J. and Clare, M.A., 2016. Large-scale sediment waves and scours on the modern seafloor and their implications for the prevalence of supercritical flows. Marine Geology, 371, pp.130-148.

50 Sequeiros, O.E., 2012. Estimating turbidity current conditions from channel morphology: A Froude number approach. Journal of Geophysical Research: Oceans, 117(C4).

51 Mountjoy, J.J., Howarth, J.D., Orpin, A.R., Barnes, P.M., Bowden, D.A., Rowden, A.A., Schimel, A.C., Holden, C., Horgan, H.J., Nodder, S.D. and Patton, J.R., 2018. Earthquakes drive large-scale submarine canyon development and sediment supply to deep-ocean basins. Science advances, 4(3), p.eaar3748.

52 Valentine, G.A., 2020. Initiation of dilute and concentrated pyroclastic currents from collapsing mixtures and origin of their proximal deposits. Bulletin of Volcanology, 82(2), p.20.

53 See supplementary materials.

54 Konsoer, K., Zinger, J. and Parker, G., 2013. Bankfull hydraulic geometry of submarine channels created by turbidity currents: Relations between bankfull channel characteristics and formative flow discharge. Journal of Geophysical Research: Earth Surface, 118(1), pp.216-228.

55 Paull, C.K., Talling, P.J., Maier, K.L., Parsons, D., Xu, J., Caress, D.W., Gwiazda, R., Lundsten, E.M., Anderson, K., Barry, J.P. and Chaffey, M., 2018. Powerful turbidity currents driven by dense basal layers. Nature communications, 9(1), p.4114.

56 Jousset, P., Currenti, G., Schwarz, B., Chalari, A., Tilmann, F., Reinsch, T., Zuccarello, L., Privitera, E. and Krawczyk, C.M., 2022. Fibre optic distributed acoustic sensing of volcanic events. Nature communications, 13(1), pp.1-16.

57 Nishimura, T., Emoto, K., Nakahara, H., Miura, S., Yamamoto, M., Sugimura, S., Ishikawa, A. and Kimura, T., 2021. Source location of volcanic earthquakes and subsurface characterization using fiber-optic cable and distributed acoustic sensing system. Scientific reports, 11(1), pp.1-12.

58 Piper, D.J. and Savoye, B., 1993. Processes of late Quaternary turbidity current flow and deposition on the Var deep-sea fan, north-west Mediterranean Sea. Sedimentology, 40(3), pp.557-582.

59 Colantoni, P., Gennesseaux, M., Vanney, J.R., Ulzeca, A., Melegari, G., Trombetta, A., 1992, Processi dinamici del canyon sottomarino di Gioia Tauro (Mare Tirreno), Giornale di Geologia, 54, pp. 190-213 Heezen and Ewing, 1952

60 Heezen BC, Ewing M. Orleansville earthquake and turbidity currents. AAPG Bulletin. 1955 Dec 1;39(12):2505-14.

61 Heijnen, M.S., Mienis, F., Gates, A.R., Bett, B.J., Hall, R.A., Hunt, J., Kane, I.A., Pebody, C., Huvenne, V.A.I., Soutter, E.L. and Clare, M.A., 2022. Challenging the highstand-dormant paradigm for land-detached submarine canyons. Nature Communications, 13(1), p.3448.

62 Shearer, P. & McClung, D. The avalanche handbook (3rd edition), Mountineers Books, Seattle, 288 pp.

References cited in Supplementary Material

63 K. Mackay. (2022). Digital Elevation Models of Hunga Volcano; pre- and post- 15 January 2022 eruption (1.0) [Data set]. Zenodo. https://doi.org/10.5281/zenodo.7456324

64 https://www.marine-geo.org/tools/files/30859 (accessed June 2023)

65 Cronin, S. J.,Brenna, M.,Smith, I. E. M.,Barker, S. J.,Tost, M.,Ford, M.,Tonga'onevai, S.,Kula, T., and Vaiomounga, R. (2017), New volcanic island unveils explosive past, Eos, 98, https://doi.org/10.1029/2017EO076589. Published on 26 June 2017.

66 Garvin et al., 2018 Monitoring and Modeling the Rapid Evolution of Earth's Newest Volcanic Island: Hunga Tonga Hunga Ha'apai (Tonga) Using High Spatial Resolution Satellite Observations Geophysical Research Letters 45. doi: 10.1002/2017GL076621

67 Talling, P. J. On the frequency distribution of turbidite thickness. Sedimentology 48, 1297–1329 (2001).

68 Brenna, M., Cronin, S.J., Smith, I.E.M., Pontesilli, A., Tost, M., Barker, S., Tonga'onevai, S., Kula, T. and Vaimounga, R., 2022. Post-caldera volcanism reveals shallow priming of an intra-ocean arc andesitic caldera: Hunga volcano, Tonga, SW Pacific. Lithos 412-413 (106614). Doi: 10.1016/j.lithos.2022.106614

69 Iacovino, K. and Till, C. B., 2019. DensityX: A program for calculating the densities of magmatic liquids up to 1,627 °C and 30 kbar. Volcanica, 2(1), pp.1–10. Doi: 10.30909/vol.02.01.0110.

70 Lange, R. A. and Carmichael, I. S., 1987. Densities of Na2O-K2O-CaO-MgO-FeO-Fe2O3-Al2O3-TiO2-SiO2 liquids: New measurements and derived partial molar properties. Geochimica et Cosmochimica Acta, 51, pp.2931–2946. doi:10.1016/0016-7037(87)90368-1.

71 Luhr, J. F., 2001. Glass inclusions and melt volatile contents at Parícutin Volcano, México. Contributions to Mineralogy and Petrology, 142, pp.261-283.

72 Vogel, A., Diplas, S., Durant, A. J., Azar, A.S., Sunding, M. F., Rose, W.I., Sytchkova, A., Bonadonna, C. and Sthol, A. Reference data set of volcanic ash physicochemical and optical properties. Journal of Geophysical Research: Atmospheres, 122(17), pp.9485-9514

73 https://www.kentik.com/blog/tonga-downed-by-massive-undersea-volcano-eruption/. Accessed 31st January 2022.

74 Stevenson, C.J., Feldens, P., Georgiopoulou, A., Schönke, M., Krastel, S., Piper, D.J., Lindhorst, K. and Mosher, D., 2018. Reconstructing the sediment concentration of a giant submarine gravity flow. Nature communications, 9(1), p.2616.

75 Belousov, A., Voight, B. and Belousova, M., 2007. Directed blasts and blast-generated pyroclastic density currents: a comparison of the Bezymianny 1956, Mount St Helens 1980, and Soufrière Hills, Montserrat 1997 eruptions and deposits. Bulletin of Volcanology, 69, pp.701-740.

76 Esposti Ongaro, T., Clarke, A.B., Voight, B., Neri, A. and Widiwijayanti, C., 2012. Multiphase flow dynamics of pyroclastic density currents during the May 18, 1980 lateral blast of Mount St. Helens. Journal of Geophysical Research: Solid Earth, 117(B6)

77 Hoblitt, R.P., 1986. Observations of the eruptions of July 22 and August 7, 1980, at Mount St. Helens, Washington (Vol. 1335). US Government Printing Office.

78 Torres, R.C., Self, S., Martinez, M.M.L., Newhall, C.G. and Punongbayan, R.S., 1996. Secondary pyroclastic flows from the June 15, 1991, ignimbrite of Mount Pinatubo. Fire and Mud: eruptions and lahars of Mount Pinatubo, Philippines, pp.665-678.

79 Scott, W.E., Hoblitt, R.P., Torres, R.C., Self, S., Martinez, M.M.L. and Nillos, T., 1996. Pyroclastic flows of the June 15, 1991, climactic eruption of Mount Pinatubo. Fire and mud: Eruptions and lahars of Mount Pinatubo, Philippines, pp.545-570.

80 Sparks, R.S.J., Barclay, J., Calder, E.S., Herd, R.A., Komorowski, J.C., Luckett, R., Norton, G.E., Ritchie, L.J., Voight, B. and Woods, A.W., 2002. Generation of a debris avalanche and violent pyroclastic density current on 26 December (Boxing Day) 1997 at Soufriere Hills Volcano, Montserrat. Geological Society, London, Memoirs, 21(1), pp.409-434.

81 Nakada, S. and Fujii, T., 1993. Preliminary report on the activity at Unzen Volcano (Japan), November 1990-November 1991: Dacite lava domes and pyroclastic flows. Journal of Volcanology and Geothermal Research, 54(3-4), pp.319-333.

82 Fujii, T. and Nakada, S., 1999. The 15 September 1991 pyroclastic flows at Unzen Volcano (Japan): a flow model for associated ash-cloud surges. Journal of Volcanology and Geothermal Research, 89(1-4), pp.159-172.

83 Behncke, B., 2009. Hazards from pyroclastic density currents at Mt. Etna (Italy). Journal of Volcanology and Geothermal Research, 180(2-4), pp.148-160.

84 Macías, J.L., Arce, J.L., García-Tenorio, F., Sosa-Ceballos, G. and Gardner, J.E., 2020. Source and behavior of pyroclastic density currents generated by Vulcanian-style explosions of Popocatépetl volcano (Mexico) on 22 January 2001. Journal of Volcanology and Geothermal Research, 406, p.107071.

85 Yamamoto, T., 2014. The pyroclastic density currents generated by the September 27, 2014 phreatic eruption of Ontake Volcano, Japan. Bull Geol Surv Japan, 65, pp.117-127.

86 Maeno, F., Nakada, S., Oikawa, T., Yoshimoto, M., Komori, J., Ishizuka, Y., Takeshita, Y., Shimano, T., Kaneko, T. and Nagai, M., 2016. Reconstruction of a phreatic eruption on 27 September 2014 at Ontake volcano, central Japan, based on proximal pyroclastic density current and fallout deposits. Earth, Planets and Space, 68, pp.1-20.

87 Komorowski, J.C., Jenkins, S., Baxter, P.J., Picquout, A., Lavigne, F., Charbonnier, S., Gertisser, R., Preece, K., Cholik, N. and Budi-Santoso, A., 2013. Paroxysmal dome explosion during the Merapi 2010 eruption: Processes and facies relationships of associated high-energy pyroclastic density currents. Journal of Volcanology and Geothermal Research, 261, pp.260-294.

88 Charbonnier, S.J., Germa, A., Connor, C.B., Gertisser, R., Preece, K., Komorowski, J.C., Lavigne, F., Dixon, T. and Connor, L., 2013. Evaluation of the impact of the 2010 pyroclastic density currents at Merapi volcano from high-resolution satellite imagery, field investigations and numerical simulations. Journal of Volcanology and Geothermal Research, 261, pp.295-315.

89 Geshi, N. and Itoh, J.I., 2018. Pyroclastic density currents associated with the 2015 phreatomagmatic eruption of the Kuchinoerabujima volcano. Earth, Planets and Space, 70(1), pp.1-12.

Acknowledgements

Non-author contributions: We thank the Kingdom of Tonga for allowing us to undertake this research and The Nippon Foundation-GEBCO Seabed 2030 project and their alumni for their support. This work would not have been possible without the captain, crew, and scientists aboard RV Tangaroa (Voyage TAN2206) and the use of SEA-KIT International's Uncrewed Surface Vessel Maxlimer for mapping the caldera. We extend our gratitude to everyone involved in these voyages and for assistance in processing the results. We thank Branko Sugar of South Sea Charters, Nuku'alofa for providing photographs of the eruption plume that are in Fig S6. The staff of the British Ocean Sediment Core Research Facility (BOSCORF), including Cian McGuire, Rebecca Garnett, Miros Charidemou and Michael Edwards, are thanked for supporting MSCL-CIS data collection and for providing logistical support to receive and store cores in the UK. We thank Rebecca Williams, two anonymous reviewers for their constructive comments and suggestions.

Funding:

Natural Environment Research Council grant NE/X00239X/1 (MAC, IAY, JEH).
Natural Environment Research Council grant NE/X003272/1 (MAC, IAY, JEH).
Natural Environment Research Council grant NE/X002454/1 (DT).
International Cable Protection Committee (MAC, IAY).
The Nippon Foundation grant: NIWA-Nippon Foundation Tonga Eruption Seabed Mapping Project (SW, RW, SS, KM, EL, MW).

Author contributions:

Conceptualization: MAC, IAY, PJT, EP, KM, RW, SW, TK, SH, CdR, MU, SK, SF, SP, DV, RR, VK

Methodology: KM, MW, IY, MAC, JEH, SF, JP, SW, SS, PJT, EP

Investigation: SS, SW, KM, MW, MAC, IAY, JEH, SC, MR

Visualization: MAC, IAY, SW, JEH, SC

Funding acquisition: MAC, IAY, JEH, MW, KM, DT

Project administration: MAC, MW, KM

Writing – original draft: MAC, IAY

Writing – review & editing: SW, RW, SS, KM, JEH, EL, PJT, EP, SC, MR, TK, DT, SH, CdR, MU, SK, SF, SP, DV, RR, VK, MW

Competing interests:

MAC is the Marine Environmental Advisor to the International Cable Protection Committee. The other authors do not have any competing interests.

Data and materials availability:

Core logs, photographs and coordinates are provided in the methods section. The pre and post-eruption bathymetric data can be accessed at 10.5281/zenodo.7456324.

Supplementary Materials

Materials and Methods
Figs. S1 to S6
Tables S1 to S5

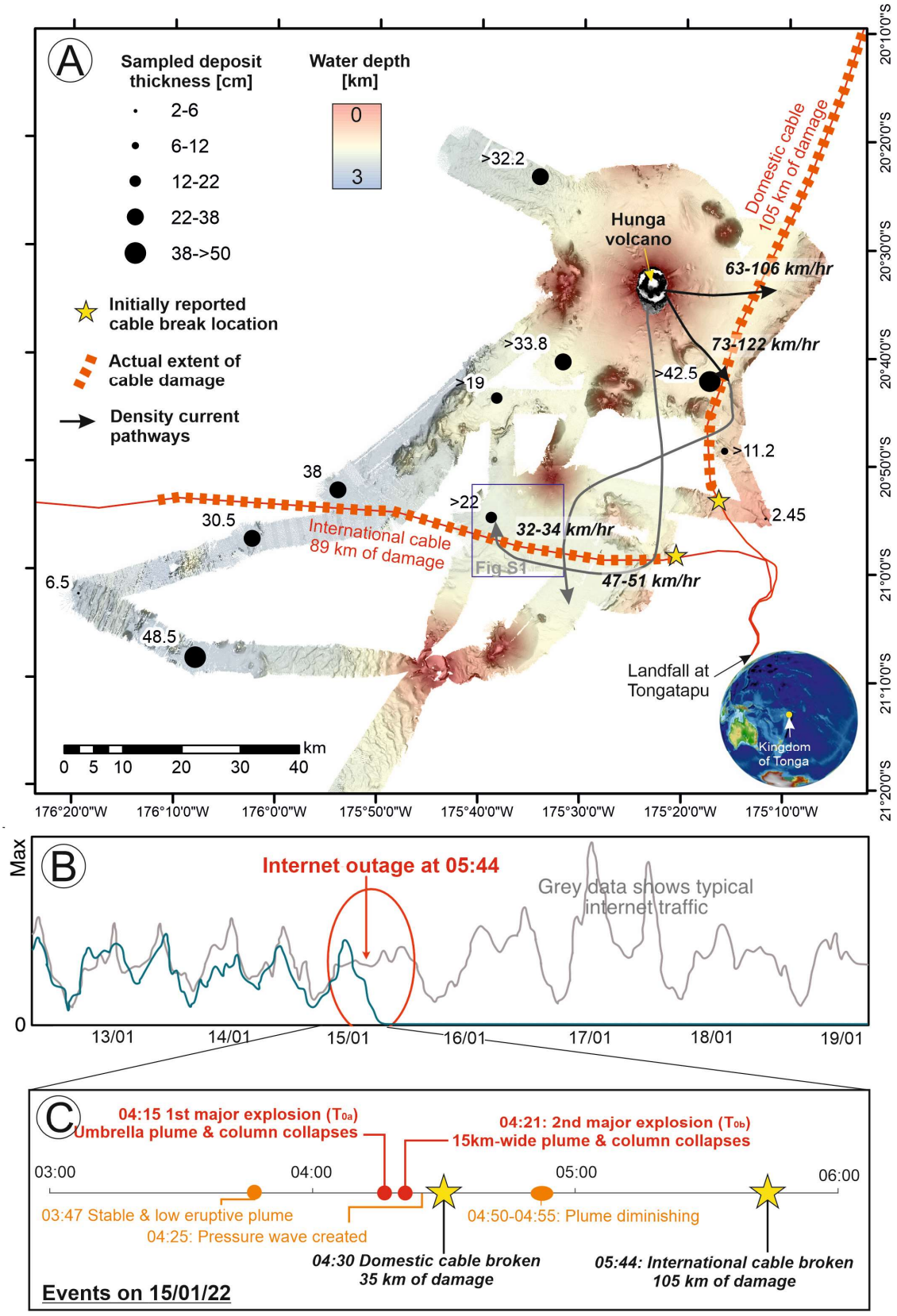
A
Sampled deposit thickness [cm]
2-6
6-12
12-22
22-38
38->50
Water depth [km]
0
3
Initially reported cable break location
Actual extent of cable damage
Density current pathways
Hunga volcano
Domestic cable 105 km of damage
63-106 km/hr
73-122 km/hr
32-34 km/hr
47-51 km/hr
International cable 89 km of damage
Fig S1
Landfall at Tongatapu
Kingdom of Tonga
>32.2
>33.8
>19
>42.5
>11.2
2.45
38
30.5
>22
6.5
48.5
km
0 5 10 20 30 40
176°20'0"W
176°10'0"W
176°0'0"W
175°50'0"W
175°40'0"W
175°30'0"W
175°20'0"W
175°10'0"W
20°10'0"S
20°20'0"S
20°30'0"S
20°40'0"S
20°50'0"S
21°0'0"S
21°10'0"S
21°20'0"S
B
Max
0
Internet outage at 05:44
Grey data shows typical internet traffic
13/01
14/01
15/01
16/01
17/01
18/01
19/01
C
04:15 1st major explosion (T0a)
Umbrella plume & column collapses
04:21: 2nd major explosion (T0b)
15km-wide plume & column collapses
03:00
04:00
05:00
06:00
03:47 Stable & low eruptive plume
04:25: Pressure wave created
04:50-04:55: Plume diminishing
04:30 Domestic cable broken
35 km of damage
05:44: International cable broken
105 km of damage
Events on 15/01/22

Figure 1: Extensive damage caused to seafloor cables by volcaniclastic density currents generated by column collapse at Hunga volcano. (A) Locations and extent of cable damage on the domestic and international seafloor cables resulting from the volcaniclastic density currents (pathways shown as arrowed lines) plotted on bathymetric data acquired three months after the eruption. The thickness of volcaniclastic density current deposits as sampled by multicoring are depicted as size-scaled solid circles, showing that these currents deposited material at least 108 km away from the caldera. Actual sampled thickness of volcaniclastic density current deposit is annotated. Where the base of the density current deposit was not sampled, this is given as >X cm. **(B)** Internet capacity shown for typical periods (in grey) compared to the sudden loss of internet traffic which flatlined at 05:44 on 15th January 2022, when the international cable was broken. **(C)** Enhanced timeline of the main eruptive phase of Hunga volcano on January 15th 2022, including the two major eruptions that caused ocean-entering column collapses. The timing of cable breaks are marked as stars, showing that they occurred after the main explosive eruptions.

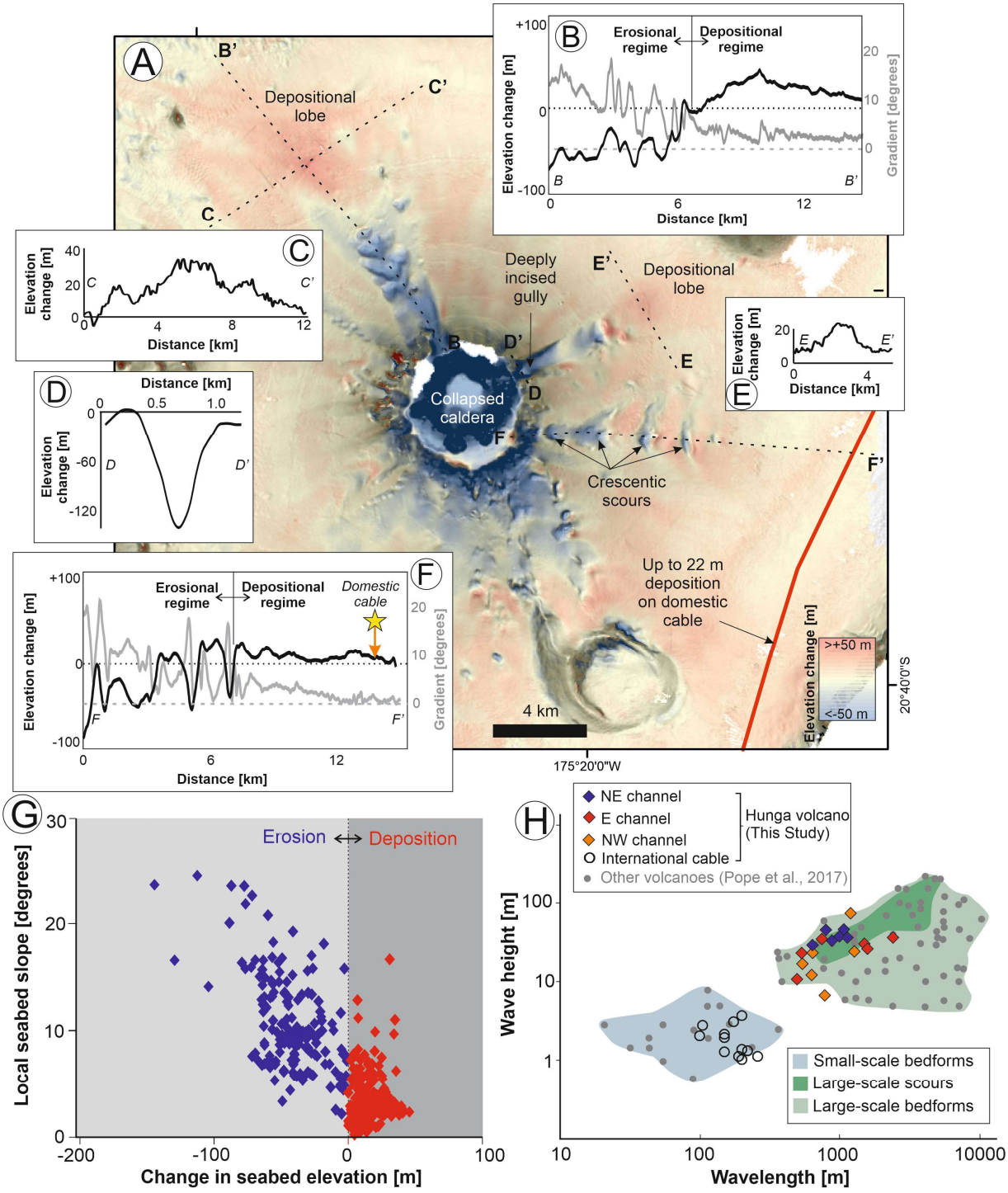

Figure 2: Sculpting of the seafloor by powerful volcaniclastic density currents on the slopes proximal to Hunga volcano. (A): Elevation difference map generated between pre- (2017) and post-eruption (April-June 2022) bathymetric surveys shows localised but major seafloor changes. The domestic cable is shown as a red line. **(B-F)**: Elevation changes shown for selected locations in cross-section, including the incision of deep (locally >120 m) gullies and upslope-migrating crescentic scours on steep (>10º) slopes (B, E & F) and the deposition of thick (up to 40 m) lobes (C&D) where slopes shallow. **(G)**: Cross plot of change in seabed elevation and local seafloor

gradient (based on pre-eruption bathymetry) to illustrate how erosion dominates on the steepest slopes, while deposition is largely restricted to slopes <10^{o}. **(H)**: Comparison of bedform morphometrics observed on the proximal flanks of Hunga volcano and around the area of the damage to the international cable with those from a database based on 17 volcanic islands worldwide (*8*) to show that the large-scale scours and bedforms plot within the range of those previously interpreted to relate to large explosive eruptions.

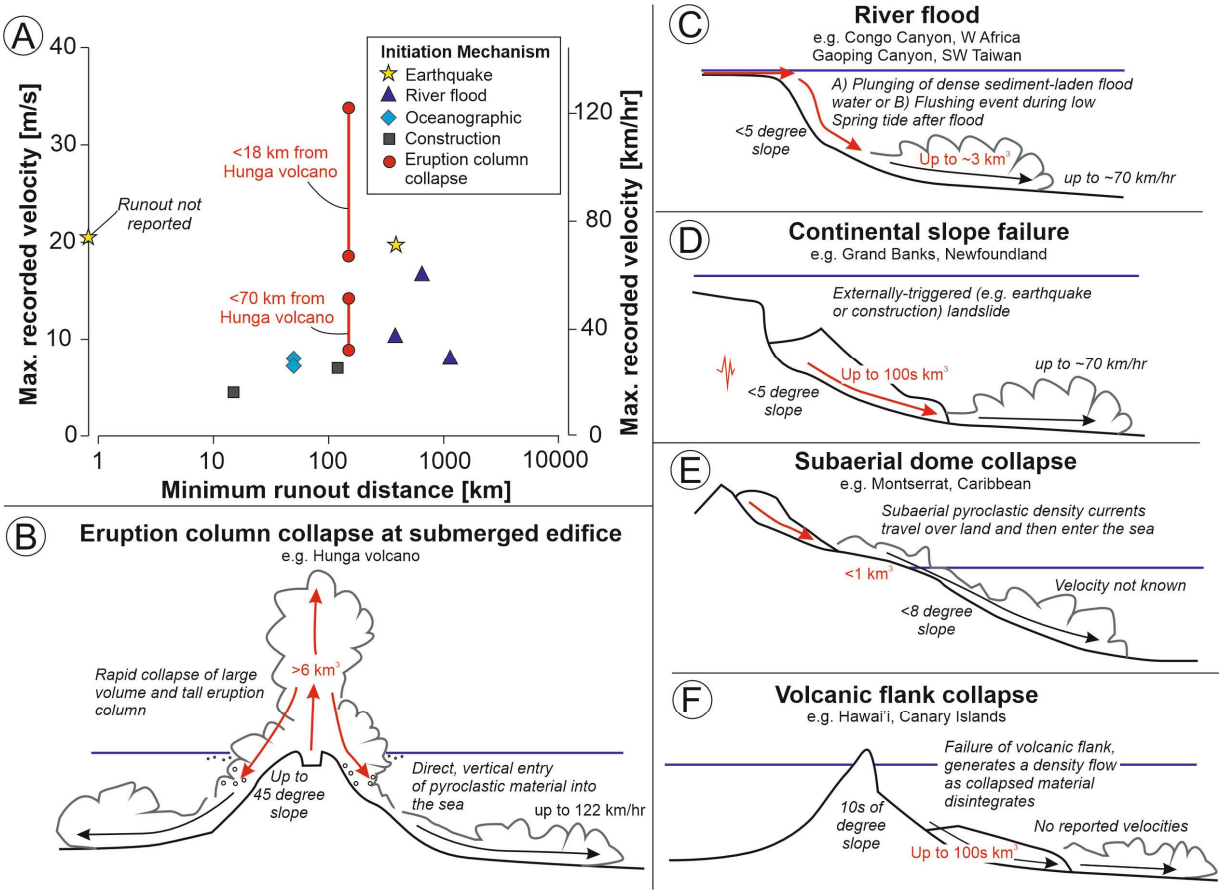

Figure 3: Density currents triggered by the Hunga volcano eruption are the fastest reported for any submerged particulate density current to date. (A) Measured velocities and minimum run-out distances for different underwater particulate density currents, symbolised relative to their triggers (as detailed in Table 1). Precise runout distances cannot be presented as often the current ran out beyond the monitoring array or the location of seafloor cables. Schematics **(B-E)** to illustrate the inception mechanisms for different submerged density currents, including: **(B)** Rapid eruption column collapse, causing vertical plunging of dense pyroclastic material onto an exceptionally steep slope as seen at Hunga volcano; **(C)** River flood triggered turbidity currents that enter the ocean either laterally (where sediment is flushed offshore) or obliquely (where dense sediment-laden flood water plunges) as observed in the Gaoping and Congo canyons; **(D)** Continental slope collapses that are initiated by external ground disturbance, such as large earthquakes or construction activity, which can initiate on very low angle slopes; **(E)** Initiated by subaerial volcanic dome collapse, entering the ocean obliquely as in the case of Montserrat; **(F)** Initiated by collapse of volcanic island flanks.

Table 1: Reported velocities of fast-moving (>4 m/s) submerged particulate density currents worldwide. Values based on sequential seafloor cable breaks or acoustic monitoring. Also compared are subaerial density currents including pyroclastic density currents and snow avalanches.

Location	Known volume	Interpreted trigger	Minimum runout distance [km]	Maximum recorded transit velocity [m/s]	Calculated velocity based on
Submarine particulate density currents including turbidity currents and volcaniclastic density					
1979 Nice Airport, Mediterranean (*58*)	0.008 km^3	Construction activity – slope failure during airport extension	120	7	Seafloor cable breaks
Gioia Canyon, Mediterranean *(41)*	Not known	Construction activity – slope failure near port	15	4.5	Seafloor cable breaks
1929 Grand Banks landslide, Newfoundland (*40*)	>200 km^3	M 7.2 earthquake triggered continental slope failure	800	19.1	Seafloor cable breaks
2006 Gaoping Canyon, Taiwan (*37*)	Not known	M 7.0 Pingtung earthquake	380	20	Seafloor cable breaks
1954 Orleansville earthquake, Algeria (60)	Not known	M 6.7 Orleansville earthquake	Not known	20.5	Seafloor cable breaks
2009 Gaoping Canyon, Taiwan (*37*)	Not known	Large river flood following typhoon	380	10.3	Seafloor cable breaks
2009 Gaoping Canyon, Taiwan (*37*)	Not known	Large river flood during typhoon	650	16.6	Seafloor cable breaks
2020 Deep-sea Congo Canyon, West Africa (*19*)	2.675 km^3	Following large river flood during low Spring tide	1130	8	Cable breaks and moored acoustic Doppler current profiler array
2015/17 Monterey Canyon, California (*55*)	Not known	Oceanographic trigger related to along shelf transport	50	7.2	Moored acoustic Doppler current profiler array

2019/20 Whittard Canyon, NE Atlantic *(61)*	Not known	Oceanographic trigger related to across shelf transport	50	8	Moored acoustic Doppler current profiler array
2022 Hunga volcano, Tonga (This study)	>6.3 km^3 (based on deposited volume on slopes outside of caldera (*15*)	Eruption column collapse	>100	33.8	Cable breaks
Subaerial particulate density currents					
Largest snow avalanches *(22, 62)*	0.01 km^3	Various	3-5	70	Radar and pressure plate measurements
Terrestrial pyroclastic density currents	Up to 5.5 km^3 for those with reported speeds but can exceed 100s km^3	Dome or flank collapse or phreatomagmatic eruption	Up to 10s of kms	7-210	See comments in Table S4 (*53*)

Science
AAAS

Supplementary Materials for

Fast and destructive density currents created by ocean-entering volcanic eruptions

Michael A. Clare[1]†, Isobel Yeo[1]†, Sally Watson[2], Richard Wysoczanski.[2], Sarah Seabrook[2], Kevin Mackay[2], James. E. Hunt[1], Emily Lane[2], Peter J. Talling[3,4], Edward Pope[3,4], Shane Cronin[5], Marta Ribó[6], Taaniela Kula[7], David Tappin[8], Stuart Henrys[9], Cornel de Ronde[9], Morelia Urlaub[10], Stefan Kutterolf[10], Samiuela Fonua[11], Semisi Panuve[11], Dean Veverka[12], Ronald Rapp[13], Valey Kamalov[14], Michael Williams[2]

[1]National Oceanography Centre, Southampton, UK
[2]National Institute of Water and Atmospheric Research (NIWA), Auckland, Aotearoa New Zealand
[3]Department of Geography, Durham University, Durham, UK
[4]Department of Earth Science, Durham University, Durham, UK
[5]School of Environment, University of Auckland, Auckland, Aotearoa New Zealand
[6]Department of Environmental Science, Auckland University of Technology, Auckland, Aotearoa New Zealand
[7]Ministry of Lands and Natural Resources, Nuku'alofa, Kingdom of Tonga;
[8]British Geological Survey, Keyworth, UK
[9]GNS Science, Lower Hutt, Aotearoa New Zealand
[10]GEOMAR Helmholtz Centre for Ocean Research Kiel, Kiel, Germany
[11]Tonga Cable Ltd, Nuku'alofa, Kingdom of Tonga
[12]Southern Cross Cable Network, North Ryde, New South Wales, Australia
[13]SubCom, Newington, NH, USA
[14]Valey Kamalov LLC, Gainsville, Florida, USA

Corresponding author. Email: michael.clare@noc.ac.uk (M.A.C.) and i.yeo@noc.ac.uk (I.Y.)
†These authors contributed equally to this work.

This PDF file includes:

Materials and Methods

Field data acquisition

Post eruption bathymetric data acquisition and coring of the density current deposits was predominantly conducted during the TESMaP expedition TAN2206 of the R/V Tangaroa to the site in April and May 2022. Bathymetric data covering the central caldera (which was too dangerous to survey with a crewed vessel) were acquired using the Uncrewed Surface Vessel (USV) Maxlimer in July – September 2022. Coring was carried out to sample the range of proximal to distal volcanic products, and to target specific locations and topographic features (including locations of damage to seafloor telecommunications cables). Tangaroa surveys were designed to maximise data acquisition efficiency between sampling sites.

Multibeam bathymetric data

Ship-based multibeam bathymetric data (*63*) were acquired using a Kongsberg EM302 multibeam echosounder operating at 30 kHz, with 288 beams (432 sounding per swath) and beam widths of 1° along- and 2° across-track. Data were acquired using the Kongsberg proprietary Seafloor Information System (SIS) acquisition software. Positioning for these surveys was provided by GPS, differentially corrected by the Fugro SeaStar XP Wide Area Differential GPS (WADGPS), heave and attitude correction was applied using Applanix POS/MV 320 motion sensor (role pitch and heading are accurate to 0.02° or better, heave is accurate to ±5% of the measured vertical displacement or ±5 cm (whichever is larger) for movements that have a measured period up to 20 s). Data were processed and cleaned using QPS Qimera v2.3.1, then gridded and exported at 50 m. Backscatter mosaics were also produced using Qimera v2.3.1, 3-sigma used to maximise contrast for the dataset and mosaics exported at the same resolution as the bathymetry (50 m). Backscatter data provide a useful identification of bedforms in deeper water areas where the scale of bedforms is close to or at the resolution of the multibeam bathymetric data (e.g. Figure S1).

USV Maxlimer multibeam data were acquired using an EM170 multibeam echosounder which operates at frequencies between 70 and 100 kHz and comprises 200 beams (400 soundings per swath) with 1° along- and across-track beam width. Real time heave and attitude data were acquired using a Seapath 130 with MRU-5+MK-11 motion sensor. USV Maxlimer was operated remotely from Essex in the UK and a team of surveyors around the world provided real time support for the multibeam acquisition. As with the ship-based data, multibeam soundings were imported into QPS Qimera v2.3.1 for processing, then gridded and exported at 50 m.

Data acquired by TESMaP after the 2022 eruption were compared with data from before this period, acquired remotely and by two separate expeditions, that were combined to form a single pre-eruption digital elevation model (DEM). Data were acquired during: i) Expedition FK160407 (May 2016) by the RV Falkor using a Kongsberg EM302 (*64*); ii) a small boat survey (November 2015) using a WASSP multibeam echosounder *(65)*; iii) satellite-derived bathymetry (2017) from Land Information New Zealand as part of the Pacific Regional Navigation Initiative (*66*). Data were imported into QPS Qimera v2.3.1 for processing, then gridded and exported at 50 m. For all surveys, sound velocity corrections were applied using sound velocity probe measurements or calculated from CTD (conductivity, temperature, depth) casts during acquisition.

Determining elevation changes between bathymetric surveys

In order to evaluate seafloor change before and after the eruption, the 50 m gridded pre- and post-eruption DEMs were co-registered and then differenced using ArcPro GIS. Other derivatives, including slope were also generated and volume differences were calculated using the Cut Fill tool. As typical vertical uncertainties on modern multibeam echosounders are around 1% of water

depth, in the survey regions this potential vertical uncertainty ranges from 20 cm in the shallowest water to 20 m in the deepest, although in many of the regions surveyed the actual measured difference between what appeared to be unimpacted regions of the volcano was < 2 m. Thus, the morphological changes appear to be well characterised by this methodology.

Coring of seafloor deposits

Coring was conducted using the Ocean Instruments MC-800 multicorer system, which were then subsampled into push-core tubes (80 cm long polycarbonate core liners). All positioning was taken from the Ultra-Short Baseline (USBL) beacon system. Cores were then cut longitudinally and parted using a cheese wire to produce a flat surface for imaging and visual core logging. Core imaging was performed using a Geotek-MSCL line scan Core Imaging System, which provides high-resolution photographic imagery. This imaging enables acquisition of precise depth-registered images. The lighting system comprises a computer-controlled high-intensity LED light array with adjustable lighting angle and light intensity for optimum imaging, particularly for wet cores. Visual logs include sedimentary structures, grain size and texture. Grain size was visually characterised through use of a grain size comparator, which has been shown by prior studies to relate to the coarsest 5% of the grain size distribution (*67*). Core sample observations were synthesised in visual sedimentological logs (Fig S2 and S3). Thicknesses of sampled deposits and core coordinates are provided in Table S2.

We differentiate between different deposits on the basis of their composition, sedimentary textures, grain size, trends in grain size variations and upper and lower contacts. This enabled us to identify and interpret four distinct facies within the sediment cores, as follows:

i) Hemipelagic deposits, which comprise ungraded, orange-brown clay-sized material with localised bioturbation. Hemipelagic deposits are inferred to be representative of background conditions, forming due to slow and steady fallout of suspended clay and silt-sized material and is typical of deep sea low energy conditions.

ii) Volcaniclastic density current deposits comprise dominantly sand to granule-sized volcanic material that generally fines upwards and (where sampled) feature a very sharp basal contact. Internal structures include abrupt changes in grain size, wavy and climbing ripple structures and fine laminations in the upper parts of the deposits. Where the base of the deposits were sampled, they overlie hemipelagic deposits. These deposits dominantly comprise lapilli (between 4 mm and 32 mm). These coarse grains comprise mafic scoria and some andesitic lithics with feldspathic phenocrysts and notable lack of olivine or clinopyroxene in the ground mass. The dominant silt to fine sand grain size is volcanic glass and scoria. This scoria is vesicular, black (grey), groundmass-dominated grains. On the basis of visual inspection, there appears to be limited presence of lithics and weathered materials. Some andesites are present, but the grains are few and far between. Another notable absence in these volcaniclastic density current deposits is the complete lack of visually discernible fauna, foraminifera and other shelled organisms. The sedimentary structures we observe are very similar to those that have been interpreted as water-entering pyroclastic density currents and the subsequent turbidity currents they created, including deposits emplaced 6-8 km from the source vent at the Pavey Ark field study *(23)* that represents deposits from a very similar volume eruption (inferred 6 km^3). At more proximal locations at Pavey Ark (<6 km from the interpreted source vent), very coarse lithic fragments, large blocks and spatter rags were seen *(23)*, however, we cannot determine whether similar deposits occur at Hunga volcano as it was not possible to sample so close to the volcano.

iii) Consistently overlying the volcaniclastic deposits is a thin veneer of orange-brown oxidised ash-rich deposits that has no obvious internal structure. These deposits are interpreted to relate to the fall out of ash following the eruption. Continued suspension and settling of ash was observed by video and sampling of the water column three months after the eruption *(15)*; hence, we consider this to be a likely explanation. However, it is possible that this deposit may instead relate to the fall out of ash-sized material that was suspended by the volcaniclastic density current as a dilute cloud and subsequently settled out after the deposition of the coarsest load of the current, or that this relates to settling from a surface plume.

iv) Volcaniclastic deposits underlying hemipelagic deposits were sampled at three locations (36-22, 76-18 and 90-23; Fig S2). These grey, well-sorted deposits comprise clay to silt-sized volcanic ash and are interpreted to relate to much older volcanic events (e.g. eruption or flank collapse events).

Density calculation

The solid density of volcanic glass can be determined from its major element chemical composition, as outlined by Lange and Carmichael (*70*). Subsequent studies (e.g.*69, 71*), modified this technique to include more recent elemental molar volumes. Notably, Vogel et al. (*72*) have shown this method to be applicable to glass-rich volcanic ash deposits. Their experiments on densities of volcanic ash samples determined by both Archimedean densitometry and theoretical calculations based on major element chemistry showed a strong agreement in results and a correlation of $r^2 = 0.94$ between the techniques. Furthermore, there was a strong correlation between silica content and density, allowing density to be predicted from silica content. Seabrook et al. (*15*) reported whole rock chemical data of nine volcaniclastic density current deposit samples from five of the cores (locations 31-20, 70-17, 83-04, 90-23 and 96-31) from this study (Figure S2). Notably, these samples are fine ash dominated samples with few phenocrysts and no visible lithic fragments, with major element compositions similar to Hunga volcano rock samples reported by Brenna et al. (*68*). Furthermore, Seabrook et al. (*15*) analysed volcanic ash sampled from the water column three months after the eruption that overlap in composition with the volcaniclastic density current material. This suggests that the volcaniclastic density current deposits were sourced from Hunga volcano, and that they are mostly glass, with only a minor mineral content. Applying the method described by Luhr (*71*), the range in density of the samples reported by Seabrook et al (*15*) is 2.64 - 2.67 g/cm3, whereas the Iacovino and Till (*69*) method gives densities of 2.62-2.65 g/cm^3. These values are similar to densities of 2.68-2.72 g/cm^3 predicted by Vogel et al.(*72*), based on sample silica content. The small discrepancy in results may be due to the errors involved but could also reflect a small proportion of higher density minerals such as olivine and pyroxene. The moderately low MgO contents of the samples (3.3 – 3.9 wt. % MgO), however, suggests high-MgO phases such as olivine and pyroxene (both of which have densities of ~ 3.2 g/cm^3) are not present in sufficient abundance to result in higher densities of the volcaniclastic density current deposit deposits. We conclude that the maximum density of the core material, based on chemical composition and likely mineral composition, is 2.8 g/cm^3.

Calculating current velocities

We determine the range of possible current velocities for a number of different plausible scenarios. In each of these we infer a start time, a distance travelled, and an arrival time. Start times are based on the intervals during which partial collapse of the eruption column was observed. To bound our calculations, we consider earliest and latest possible start times (T0) that span from T0a (at 04:15 UTC) when a possible low pyroclastic density current cloud was observed to T0b (at 04:21 UTC)

when the main plume started to collapse and pyroclastic material was observed to enter the sea *(34)*. The distance travelled by the currents is based on numerical modelling of density currents in Seabrook et al. (*15*). which includes more direct as well as more tortuous pathways to also provide upper and lower bounds on the derived velocity. Finally, we take the arrival time at the subsea cables based on the timing of reported loss of communication on each of the cables (*73*), which is accurate to the minute.

Comparison with other subaerial pyroclastic density currents

In order to place the velocities calculated for the volcaniclastic density currents in a wider context, in Table S2 we present a summary of previously reported flow speeds and volumes for pyroclastic density currents on land.

Estimation of current properties: Thickness and sediment concentration

We infer estimates of depth-averaged sediment concentration using the modified Chézy formulation, assuming different current thicknesses, and based on observed slope angles (measured from multibeam bathymetric data) and calculated current speed (based on cable breaks) (Table S5). This simplified depth-averaged approach is commonly applied to determine properties for turbidity currents(e.g. *54, 74*). It is important to acknowledge that the modified Chézy formulation we use was not developed for modelling very dense flows (where grain to grain interactions occur), nor does it account for density stratification, nor temperature effects that may modify the density of the flow. As a consequence, this approach simply provides some first order estimates of plausible ranges of flow properties for the density currents offshore Hunga volcano. Future depth-resolved modelling may enable more realistic estimates of flow properties.

Using the modified Chézy formulation, the depth-averaged velocity, U, is derived through:

$$U^2 = \frac{RCgH_f sin\theta}{C_d + E_w}$$

where R is the submerged specific gravity of the sediment in seawater, taken here as the value for andesite (1.8). C is the depth averaged sediment concentration of the density current, g is the gravitational acceleration, H_f is the height of the velocity maximum above the seafloor (25% of the total current thickness), S is the slope gradient, Θ is the slope angle, E_w is the water entrainment coefficient across the upper current interface ($0.072 sin\Theta/1000$) and Cd is the basal friction coefficient (here assumed as 0.005 based on Konsoer et al. (*54*). R is derived as:

$$R = \frac{\rho_o - \rho_f}{\rho_f}$$

where ρ_o is the density of the grains and ρ_f is the density of seawater.

We can solve the modified Chézy equation to determine plausible ranges of current thickness and sediment concentration using the velocity calculated from cable breaks. Cable breaks provide a measure of the maximum frontal velocity of a density current, which has been shown to be approximately five times that of the depth-averaged current velocity (*74*). We therefore solve this equation for a depth-averaged velocity of 7.8 m/s (i.e. one fifth of the maximum calculated transit current velocity of 38.8 m/s). The derived flow thicknesses from this simple modelling do not

relate to the resultant deposit thicknesses, as much of the flow will likely bypass and the location and rate of deposition is controlled by local topography, flow speed and other variables not accounted for in this modelling.

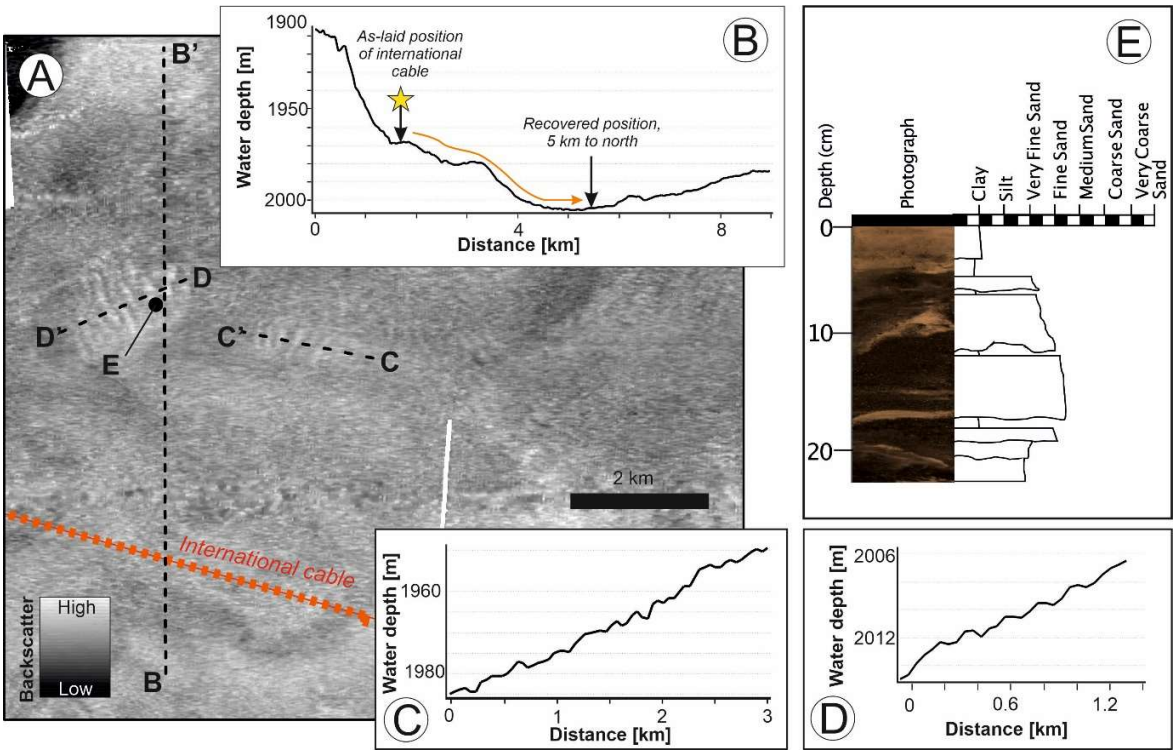

Fig S1: Evidence of seafloor current >70 km from Hunga volcano as shown by cable damage and displacement and bedforms. (A) Seafloor backscatter acquired a Kongsberg EM302 multibeam echosounder, showing evidence of small-scale bedforms that are typically observed in settings affected by turbidity currents. The original location of the international cable is annotated. **(B)** Bathymetric cross section to illustrate the valley which provided a topographic steer to the density current, which is interpreted to have damaged and relocated the international cable as shown. **(C & D)** Bathymetric profiles illustrating small-scale upstream asymmetric bedforms that provide evidence of seafloor working by a sediment density current. **(E)** Multicore 83-04 acquired at location as shown in Panel A that sampled part of a sediment density current deposit that is rich in pyroclastic material, but which did not reach the base of the deposit.

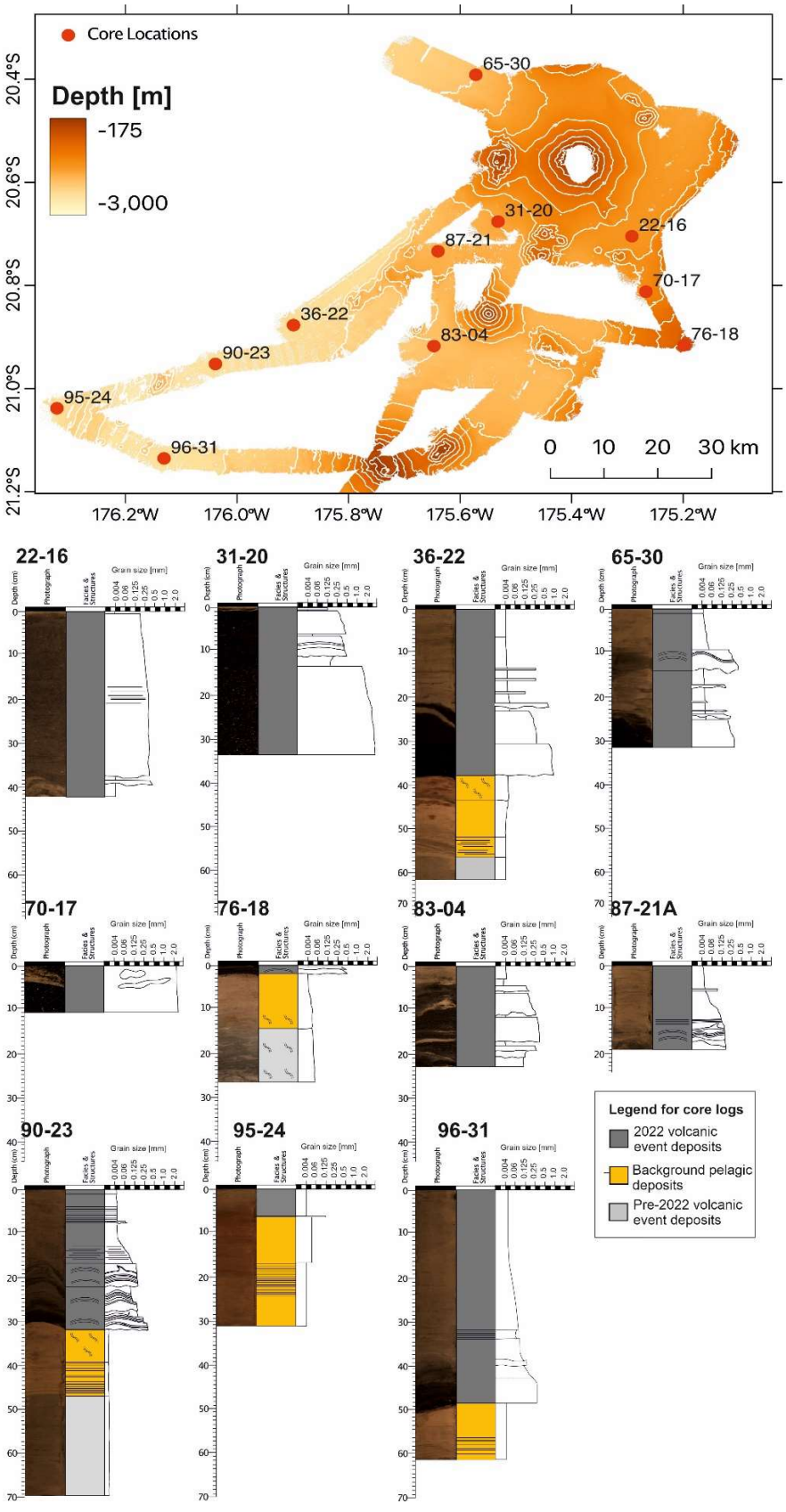
Core Locations
Depth [m]
-175
-3,000
65-30
31-20
22-16
87-21
70-17
36-22
76-18
83-04
90-23
95-24
96-31
0 10 20 30 km
20.4°S
20.6°S
20.8°S
21.0°S
21.2°S
176.2°W
176.0°W
175.8°W
175.6°W
175.4°W
175.2°W
22-16
31-20
36-22
65-30
70-17
76-18
83-04
87-21A
90-23
95-24
96-31
Legend for core logs
2022 volcanic event deposits
Background pelagic deposits
Pre-2022 volcanic event deposits

Fig S2: Seafloor cores used in this study. Top panel shows core locations (red circles) over pre-eruption bathymetry shown as colour wash with 500 m contours in white. Lower panels show visual core logs annotated with volcanic deposits interpreted to result from the 2022 eruption (dark grey), background sedimentation (yellow) and pre-2022 eruption deposits (light grey). Grain size was visually characterised through use of a grain size comparator, which has been shown by prior studies to relate to the coarsest 5% of the grain size distribution (*67*).

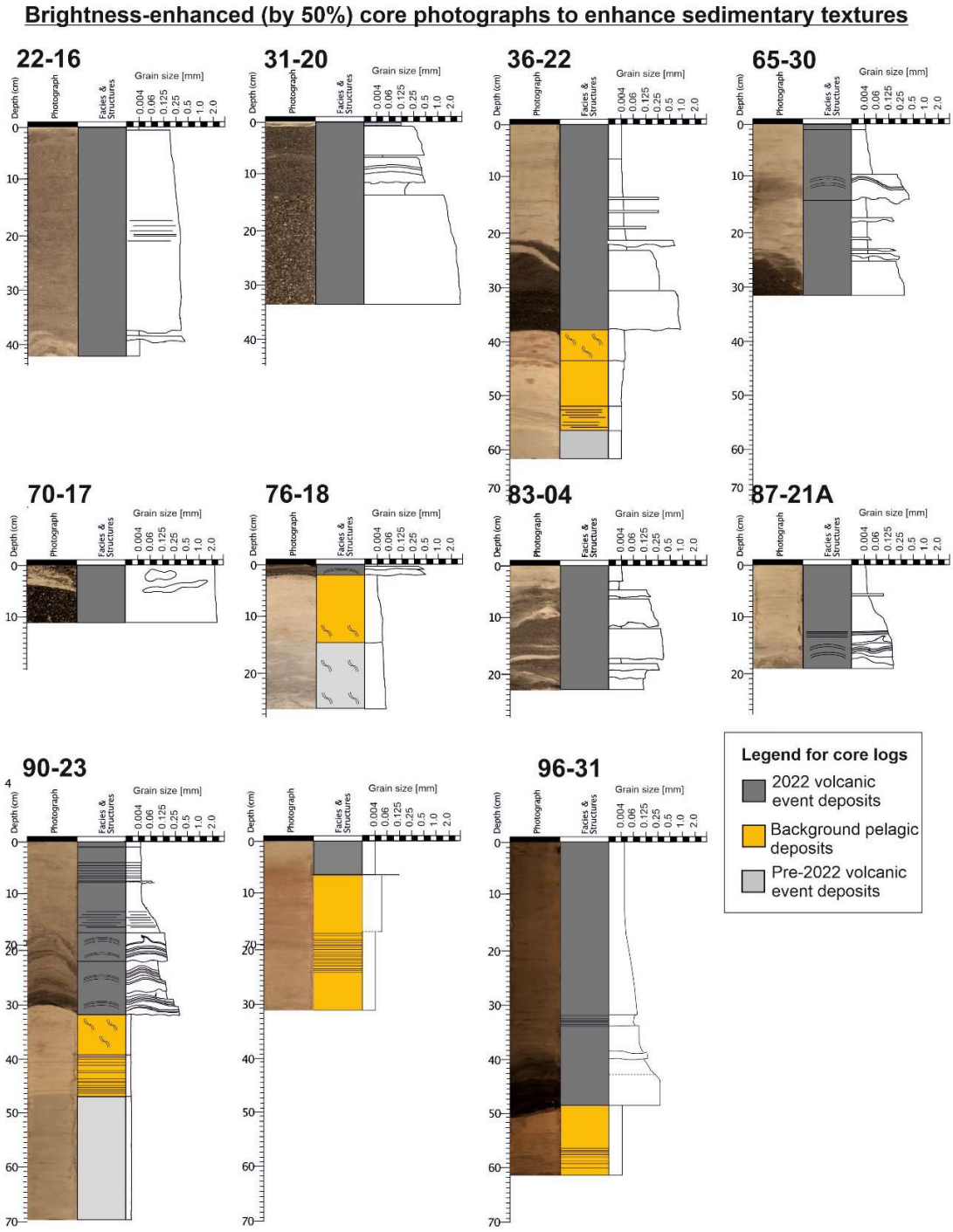

Fig S3: Enhanced photographs of sediment cores to show sedimentary features more clearly. Shown here is a replication of the core logs from Figure S2 but with the photographs brightened artificially by 50% to enhance the detail that cannot easily be seen for very dark sediments. Grain size was visually characterised through use of a grain size comparator, which has been shown by prior studies to relate to the coarsest 5% of the grain size distribution (*67*).

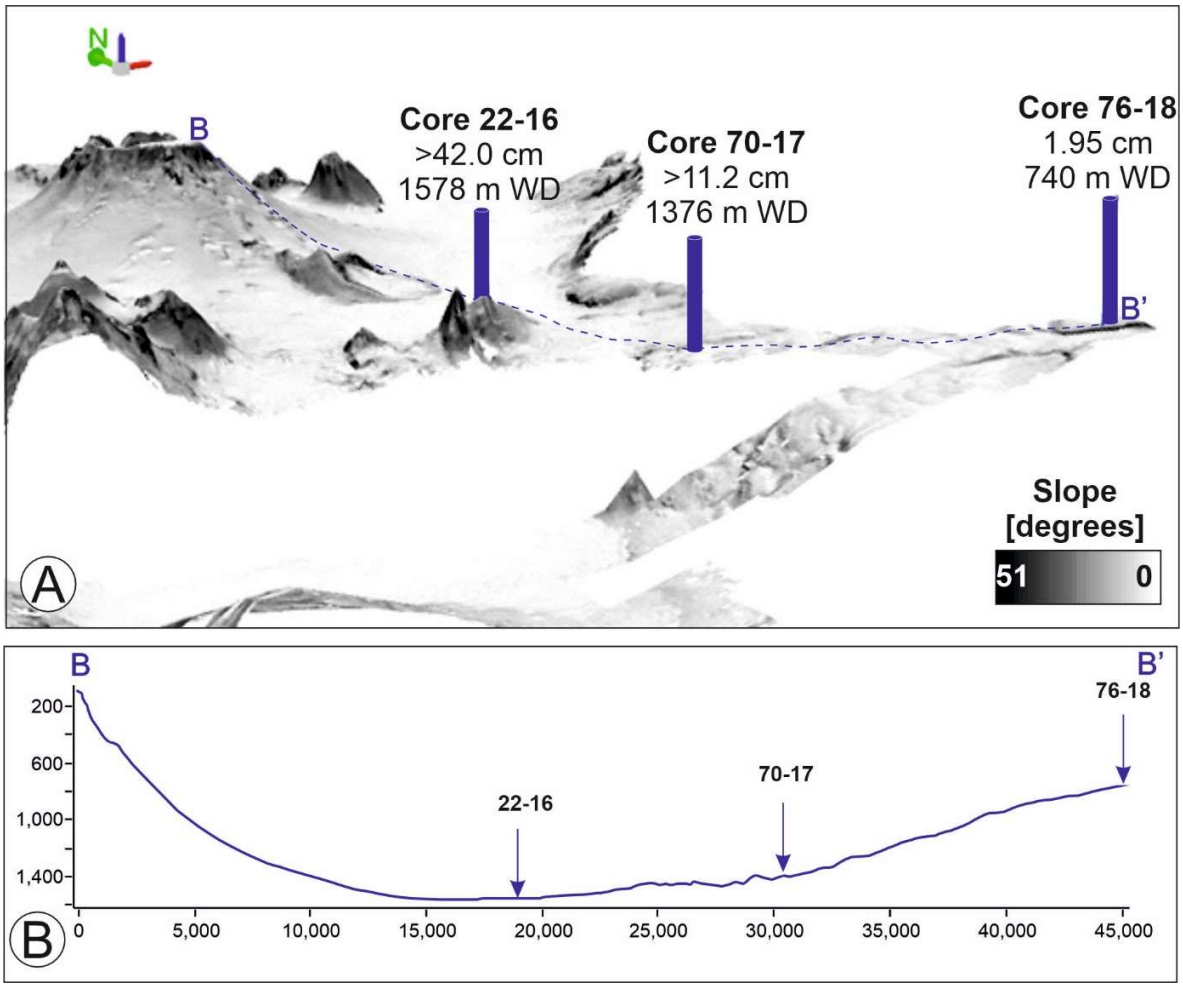

Fig S4: South-west coring transect reveals elevation gained by volcaniclastic density currents. (A) A four-times vertical exaggerated three-dimensional rendering of the bathymetry annotated with the locations of the south-west transect of seafloor coring locations. The core name, the thickness of volcaniclastic density current deposits sampled, and the water depth (WD) are each location are labelled at each of the three coring locations along the transect. **(B)** The bathymetric profile along the transect B-B' shown in Panel A with core locations annotated. Density currents were capable of travelling upslope, from around 1600 m to at least 740 m water depth.

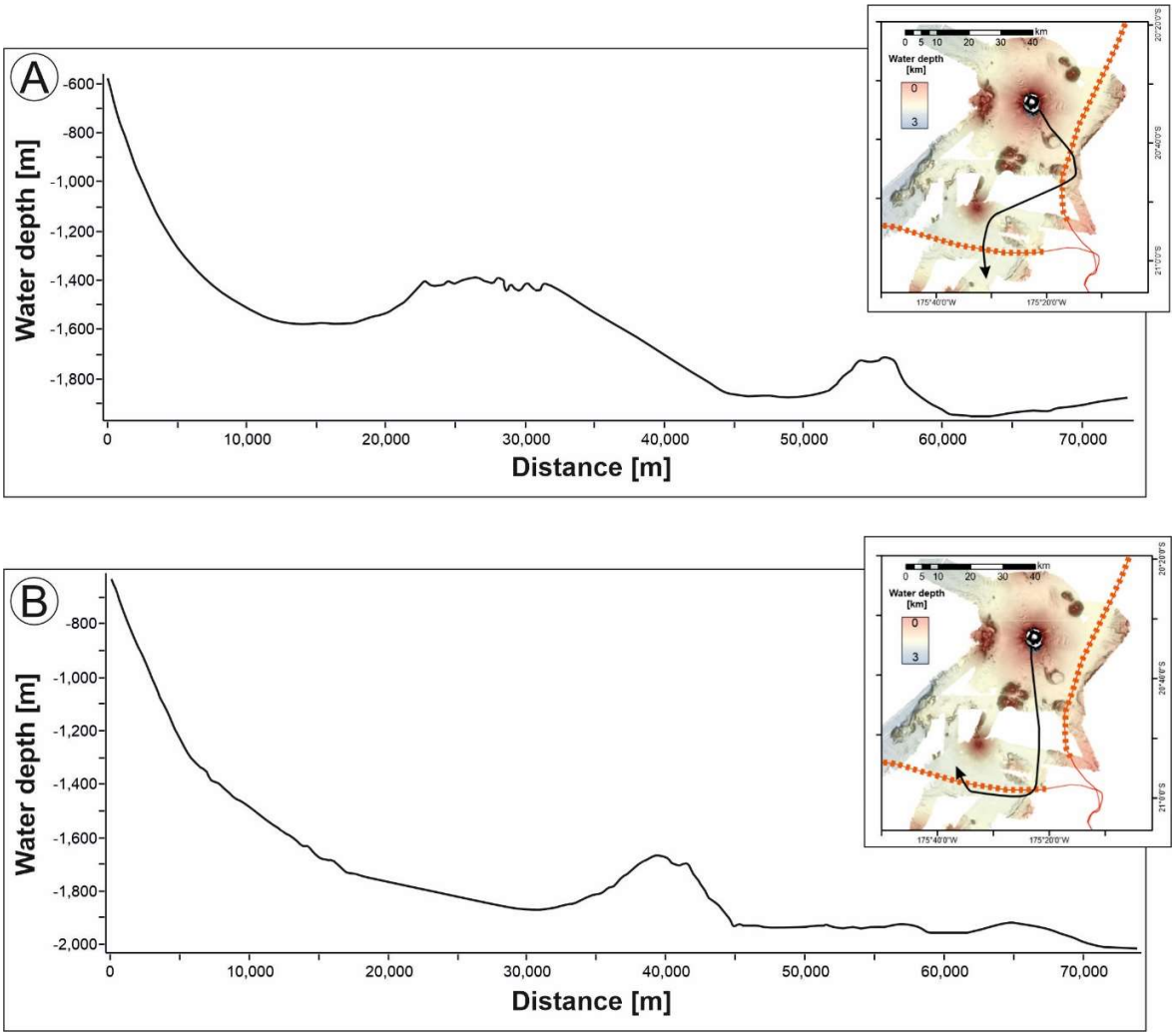

Fig S5: Bathymetric profiles along inferred pathways of volcaniclastic density currents. (A) The inferred pathway of a current that initially travelled south-westward from Hunga volcano. **(B)** The inferred pathway of a current that initially travelled southward. Inset figures show those inferred flow pathways and the locations of the seafloor cables overlain on the bathymetric data (as presented in more detail in Fig. 1). Currents initially travelled downslope, but then traversed across several hundred meters of positive relief for part of their journey.

Images of the eruption plume taken approximately 10 km NE of Tongatapu by Branko Sugar (South Sea Charters, Nuku'alofa)

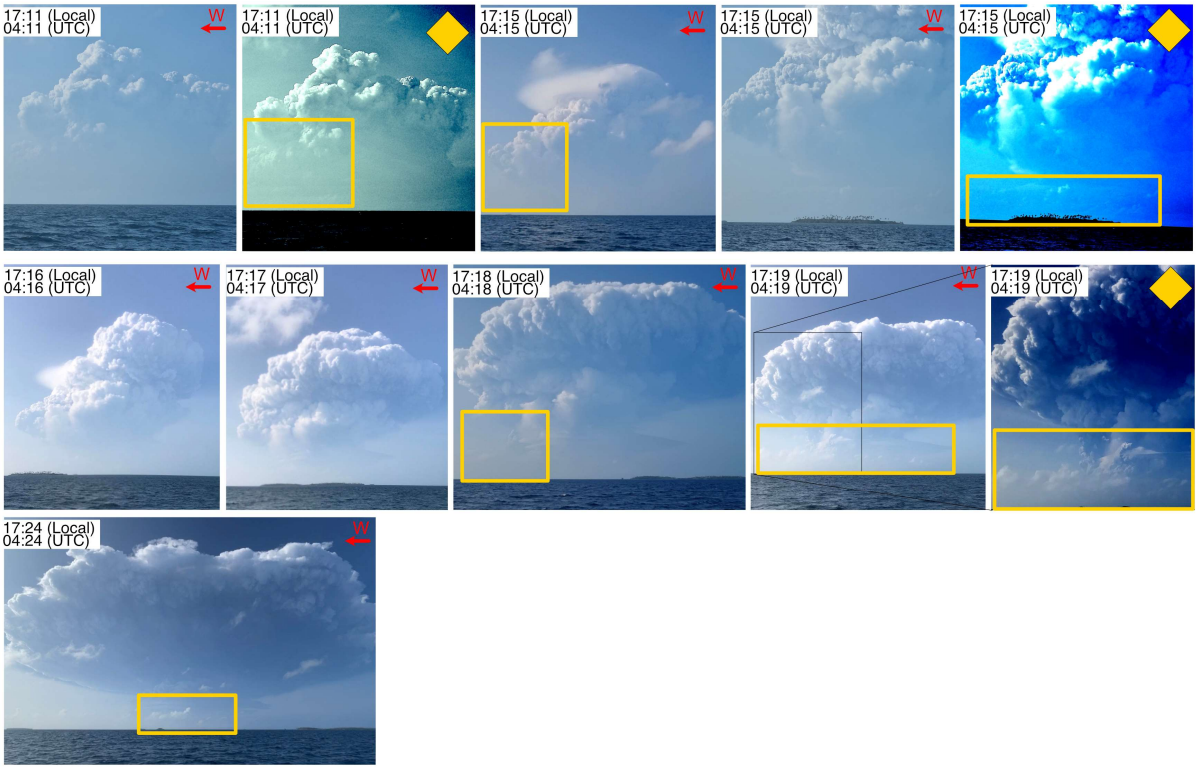

Fig S6: Photographs taken in the immediate aftermath of the eruption by Branko Sugar from South Sea Charters, Nuku'alofa, using a mobile phone. Images which have had the contrast or colors enhanced to make features in the eruption plume clearer are denoted by a yellow diamond. Red arrows point westward. The images at 17:11 local time (04:11 UTC) show the very first small explosive event and the beginning of the formation of minor regions of column collapse can be observed on the western side of the plume (yellow squares). These collapses are relatively small, similar to those observed during the first phase of this eruption that started in December 2021, and occur on the western side, away from the domestic telecommunications cable. Following the larger explosion at 17:15 local time (04:15 UTC) the column grows substantially and large volumes of material begin to collapse from the margins into the ocean (yellow squares). While the first collapses of the larger column are seen at 17:15 local time (04:15 UTC), it can also be observed in images taken at 17:18 (04:18 UTC), 17:19 (04:19 UTC) and 17:24 (04:24 UTC). In these images collapse does not appear to be limited to the western side, although the eastern side is hazier in the images and harder to make out. We are not in possession of images taken beyond 17:24, but it is likely column collapse continued beyond the period shown here.

Table S1: Calculated velocities for the volcaniclastic density currents based on distance to and timing of cable breaks. The ranges presented are based on the collapse of the eruption column into the ocean during different stages in the main eruptive phase, either during $T0_a$ (at 04:15 UTC) when a low collapse cloud was observed or $T0_b$ (at 04:21 UTC) when the main plume started to collapse. As the precise current pathways are not known, the distance is measured along different plausible current pathways (based on previous modelling of pathways (*15)* shown in Fig 1). The timing of cable breaks is known to the nearest minute with the domestic cable being cut at 04:30 UTC and the international cable at 05:44 UTC.

Current pathway scenarios	**Distance along current pathway [m]**	**Minimum velocity based on inception at T_{0a} [m/s]**	**Maximum velocity based on inception at T_{0b} [m/s]**	**Minimum velocity based on inception at T_{0a} [km/hr]**	**Maximum velocity based on inception at T_{0b} [km/hr]**
Damage to domestic cable					
F1A: E path	15867	17.6	29.4	63.5	105.8
F1B: SW path	18271	20.3	33.8	73.1	121.8
Damage to international cable					
F2A: SE path	70071	13.1	14.1	47.2	50.7
F2B: S path	47133	8.8	9.5	31.8	34.1

Table S2: Summary of seafloor samples. The samples were recovered using a multicore, detailing core locations and recovered thicknesses of ash fall and density current deposits linked to the January 2022 Hunga volcano eruption. Where thickness values of >X cm are shown, this is where the base of the deposit was not recovered and extends below the depth limit of sampling.

Core site name	Latitude	Longitude	Water depth [m]	Core recovery [cm]	Ashfall + density current deposit thickness [cm]	Ashfall deposit thickness [cm]	Density current deposit [cm]
76-18	-20.9160	-175.1985	740	25.4	2.45	0.5	1.95
70-17	-20.8123	-175.2670	1376	11.2	>11.2	0.0	>11.2
22-16	-20.7047	-175.2922	1555	42.5	>42.5	0.5	>42.0
31-20	-20.6763	-175.5322	1718	33.8	>33.8	1.0	>32.8
65-30	-20.3915	-175.5720	2068	32.2	>32.2	4.5	27.7
87-21A	-20.7338	-175.6398	1860	18.5	>18.5	5.8	>12.7
83-04	-20.9177	-175.6472	2000	22.0	>22.0	3.0	>19.0
36-22	-20.8772	-175.8988	2330	62.0	38.0	4.0	34.0
90-23	-20.9525	-176.0388	2412	69.5	30.5	7.5	23.0
96-31	-21.1357	-176.1310	2411	61.5	48.5	1.5	47.0
95-24	-21.0385	-176.3230	2449	31.4	6.5	2.0	4.5

Table S3: Descriptions for sediment cores logged in this study. These descriptions supplement visual core logs provided in Figure S2.

Core location	Recovered length (cm)	Descriptive comments
90-23	69.5 cm	0-1 cm Brown-orange fine clay with evidence of oxidation. 0-6 cm Grey-brown clay to very fine silt. 6 cm Notable change in yield strength and water saturation. 6-7.5 cm Very fine wisp of black volcaniclastic silt. 7.5-16.4 cm Graded interval of very fine sand to silt to clay-fine silt. Grey-brown colour with mostly discontinuous laminations remaining mostly structureless. 16.4-28.0 cm Boundary as grain-size break from structured sand to graded but structureless sand-silt. Interval has ripple-laminated very fine sand. Ripples are distorted with possible flame structures. 28.0-29.3 cm Dark grey fine volcaniclastic sand with onlapping ripple laminations. 29.3-30.5 cm Interval of fine-medium sand, black volcaniclastic lens. Interval to base of Hunga 2022 deposit. 30.5-40.8 cm Interval of orange-brown clay with heavy bioturbation. There is a patchy fabric to the sediment with uneven distribution of sand particulate throughout. 40.8-46.6 cm Boundary to very fine silt stringer demarking upper boundary of interval. Interval of very fine silt orange-brown laminations of orange-red colour. 46.6-54.0 cm Interval has subtle discontinuous laminations. 54.0-62.0 cm Interval of grey-brown clay-silt. 62.0-69.5 cm Interval od grey-brown clay-silt to core base.
96-31	61.5 cm	0-1.5 cm Interval of orange to brown-grey clay. 1.5-32.0 cm Interval of graded, water saturated grey clay-to-fine silt. There are wisp of discontinuous silt laminations throughout, often convoluted. 32.0-34.0 cm Interval of laminated silts, graded.

		34.0-43.0 cm Graded and laminated black, ripple convoluted volcaniclastic sand. 43.0-48.5 cm Ripple laminated, black volcaniclastic ungraded from base of Hunga 2022 deposit. 48.5-57.0 cm Interval of orange-brown to brown-grey bioturbated clay. 57.0-59.8 cm Interval of laminated orange-brown clay, where the laminations are red, potentially iron-stained. 59.8-61.5 cm Grey-black silty clay.
22-16	42.5 cm	0-0.5 cm Orange-brown clay-silt above a basaltic sand. 0.5-37.0 cm Interval of ungraded uniform, black, volcaniclastic, fine sand. Deposit interval has crude discontinuous laminations throughout. 37.0-42.0 cm Interval of convolute laminations within dark volcaniclastic sand with layers of more oxidised brown-grey silt-sand. 42.0-42.5 cm Brown-grey clay below sand.
87-21A	18.5 cm	0-1.4 cm Interval of brown-grey clay to very fine silt lighter in colour than below. 1.4-5.4 cm Interval has bioturbation containing silt-sized particulate. Above 3.0 cm there are subtle contortions. The interval has evidence of fine <1 mm-scale laminations below 4.4 cm, above which the sediment is generally structureless and massive. 5.4-5.8 cm Interval formed structureless sediment. 5.8-13.0 cm mm-thick stringer of black volcaniclastic sand. 13.0-14.3 cm Interval of near-continuous laminations <1 mm thick. 14.3-18.5 cm Interval is very fine sand but with notable clay content. Here there are >1mm scale laminations, with evidence of climbing ripple sets. There a potentially a post deposition deformation structure present as a set of contortion.
83-04	22.0 cm	0-0.2 cm Orange clay. 0.2-3.0 cm Graded brown-grey clay-silt. 3.0-4.0 cm Grey-brown clay.

		4.0-5.4 cm Structureless black volcaniclastic sand. 5.4-5.5 cm Clay-silt layer. 5.5-8.0 cm Interval of convolute laminated black volcaniclastic sand. 8.0-8.8 cm Interval of clay-silt. 8.8-16.0 cm Upper bound of grain-size break to rippled clay-silt with potential flame structure. Interval was a very well sorted, structureless, black sand. Weak upwards fining. 16.0-16.8 cm Laminated brown-grey clay with grain size break. 16.8-18.0 cm Coarsening-upwards volcaniclastic sand with upper bound terminating in a grain size break. 18.0-22.0 cm Interbedded fine black volcaniclastic sand and clay laminations containing ripples and distorted ripples in places.
65-30	32.2 cm	0-1.0 cm Interval of orange-brown clay with silty bioturbation. 1.0-4.5 cm Brown-grey clay with fine bioturbation infilled with silt particulate. 4.5-10.0 cm Very fine brown-grey clay with indistinct discontinuous laminations. 10.0-17.6 cm Ungraded very well sorted brown-grey clay with laminations above a sand stringer. 17.6-21.5 cm Graded brown-grey clay. 21.5-24.2 cm Graded and laminated grey silt above ripple laminations. 24.2-25.2 cm Interval of ripple laminated clay and black volcaniclastic sand. 25.2-32.2 cm Graded black-grey volcaniclastic fine-to-medium sand.
95-24	31.4 cm	0-2.0 cm Orange-brown clay. 2.0-6.5 cm Water saturated orange-brown clay above a 1 mm black volcaniclastic silt layer. 6.5-17.5 cm Bioturbated orange-brown clay with distributed silt.

		17.5-24.5 cm Interval of orange-brown clay, which is very well sorted with fine <1 mm-scale laminations with red staining. 24.5-31.4 cm Orange-brown clay which is very well sorted and contains discontinuous laminations.
70-17	11.2 cm	0-1.8 cm Injected volcaniclastic black sand. 1.8-4.5 cm Brown-grey clay with a <1 mm-thick layer of fine volcanic sand at 2.8 cm. 4.5-6.0 cm Very coarse volcaniclastic sand with an upper bound to a clay. 6.0-8.0 cm Interval of coarse volcaniclastic sand coarsening upwards. 8.0-11.2 cm Fining upwards very coarse, black volcaniclastic sand. No notable bioclasts.
31-20	33.8 cm	0-1.0 cm Orange-brown clay. 1.0-6.6 cm Well-sorted black volcaniclastic medium sand. 6.6-7.0 cm Interval of fine grey silt. 7.0-13.8 cm Black volcaniclastic medium sand with distinct coarsening-upwards fabric to upper bound. 13.8-33.8 cm Weakly graded black volcaniclastic sand containing mixture of scoria and glass. Relatively well sorted.
36-22	62.0 cm	0-1.0 cm Orange-brown clay. 1.0-14.5 cm Fine laminated grey clay with <1 mm-thick black silt stringers at 4.0 cm and 7.0 cm. 14.5-21.5 Laminated fine silt graded to clay with discontinuous laminations. 21.5-23.0 cm Very well sorted black volcaniclastic sand. 23.0-24.0 cm Brown-grey clay. 24.0-31.0 cm Ungraded, black volcaniclastic sand with convoluted ripple laminations. 31.0-38.0 cm Very well sorted, black, volcaniclastic sand with sharp base above an orange-brown clay. 38.0-56.0 cm Orange-brown bioturbated clay.

		56.0-62.0 cm Fine clay interval, structureless and grey in colour.
76-18	25.4 cm	0-0.5 cm Orange-brown clay 0.5-1.2 cm Graded black volcaniclastic sand with horizontal laminations. 1.2-2.4 cm Black volcaniclastic sand with distinct ripple laminations. 2.4-13.0 Pale white-orange bioturbated clay with sporadic distributed basaltic grains. 13.0-21.2 cm Lower interval of white-orange bioturbated clay.

Table S4: Documented velocities of pyroclastic density currents on land, reporting additional information where is available on volumes.

Volcano	Date	Velocity and volume	Supporting data	Comments
Mt. St. Helens (*75*)	March 27, 1980	~130–210 m/s 2.5 km^3 (dome volume)	Photographic and satellite observations with max speed inferred as 1.43*speed of head	Initial internal velocities (max observed head velocities 100 - 110 m/s initially remaining > 90 m/s for several minutes). 210 m/s is a peak ejection velocity.
Mt. St. Helens (*76*)	May 18, 1980	175 (initial blast velocity) – 40-50 m/s Magma and non-juvenile material assumed to be incorporated at the source (90 × 10^6 m^3 and 60 × 10^6 m^3 of dense rock equivalent, respectively)	Numerical simulation	Initial blast velocities resulted in very high initial velocities which slowed to 150 m/s after 60s and 40-50m/s after 120s.
Mt. St. Helens (*77*)	7 August 1986	30 m/s	Photographic and satellite observations	Smaller current, flow front speed
Pinatubo (*78,79*)	1993	Few m/s 5.5 km^3	Visual observations/ inferred from explosions	Secondary pyroclastic currents caused by collapse of ignimbrite sheet
Soufriere Hills (*80*)	August 4-12 and September 22 - October 22, 1997	83 – 60 m/s (80 – 120 m/s internal velocities) 1.8 - 3.2 x 10^6 m^3 (on land) total pyroclastic density current deposits, 35 -	Field observations/film recordings	Initial speeds for dome collapse flows, slowing to 10 m/s or less (90 m/s observed for surges)

		45 x 10^6 m^3 material that formed the pyroclastic density current		
Soufriere Hills (*75)*	26 December 1997	79 – 54 m/s 1.8 - 3.2 x 10^6 m^3 (on land) total pyroclastic density current deposits, 35 - 45 x 10^6 m^3 material that formed the PDC	Field observations/film recordings with max speed inferred as 1.43*speed of head	Internal speed (observed frontal speeds 38 – 57 ms^{-1})
Unzen (*81,82*)	November 1990-November 1991	28 – 14 m/s 1 × 10^6 m^3 Dense Rock Equivalent	Field observations and time lags between the start of the seismic tremor and the destruction of equipment.	Small dome collapse pyroclastic density currents (frontal speeds)
Etna (*83*)	1986-2006	33 - 14 m/s	Field observations and reports, photographs and video footage, footage of the monitoring video cameras	Small eruptions (frontal speed)
Popocatépetl (*84*)	22 January 2001	30 - 7 m/s 5.71 × 10^5 m^3 total non Dense Rock Equivalent deposit volume	Video footage	Lower number is minimum speed (frontal speed)
Ontake (*85,86*)	27 September 2014	8 – 28 m/s 0.036 –0.072 × 10^6 m^3 pyroclastic density current deposits	Video footage	Phreatic Frontal speed Up to 28m/s estimated from deposit characteristics

Merapi 2010 (*87,88*)	29 October–23 November 2010	128 m/s fastest velocity non- Dense Rock Equivalent deposit volume is ~ 36.3×10^6 m^3 with 70% deposited during a single eruptive phase 4-5 November	Damage to a station at a known distance from source	None
Kuchinoerabujima (*89*)	29 May 2015	42 m/s 1.1×10^5, 3.8×10^4, and 3.6×10^4 m^3, respectively in the Zones e, d, and c, total Dense Rock Equivalent 2.4×10^8 kg	Monitoring cameras	Phreatomagmatic, average speed

Table S5: Inference of flow properties for different assumed depth-averaged sediment concentrations on different slope angles based on application of the Chézy equation. The slope values shown are representative of the slopes found along the course of the volcaniclastic density currents, with slopes of 10-20° degrees occurring on the edifice flanks, and slopes of 1-5° representing conditions further from the volcanic edifice. Upper values for concentration are based on inferences from prior studies of turbidity currents *(74)* and collapsing eruption plumes *(52)*.

Depth-Averaged Sediment Concentration, C	Slope [degrees]	Height of velocity maximum above seafloor, Hf [m]	Flow thickness [m]
1%	20	5	21
	10	11	42
	5	21	84
	2	52	208
	1	104	416
2%	20	3	10
	10	5	21
	5	11	42
	2	26	104
	1	52	208
5%	20	1	4
	10	2	8
	5	4	17
	2	10	42
	1	21	83
10%	20	<1	2
	10	1	4
	5	2	9
	2	5	21
	1	10	42